RECEIVER SYNCHRONIZATION FOR THE OPPORTUNISTIC USE OF INTEGRATED SERVICE DIGITAL BROADCASTING - TERRESTRIAL DIGITAL TELEVISION SIGNALS

BY

BERAT LEVENT GEZER

THESIS

Submitted in partial fulfillment of the requirements
for the degree of Master of Science in Electrical and Computer Engineering
in the Graduate College of the
University of Illinois at Urbana-Champaign, 2019

Urbana, Illinois

Advisers:

Professor Steven J. Franke
Professor Farzad Kamalabadi

ABSTRACT

Opportunistic use of signals has become a method that is resorted to in research, and industry for various reasons. Although they come with some challenges which can be overcome by applying different techniques, a great number of advantages brought to the field by these signals have made their use practical. Some of these signals like digital television are transmitted at high power. The Ionospheric Scintillation Explorer (ISX) mission dedicated to studying the ionospheric scintillations has been suggested by SRI International, Inc., as a satellite which will receive the trans-ionospheric digital television signals. In order to understand the spatial extent of the scintillating flux tubes, cross-correlation of the phase and amplitude of the pilot carriers in the digital television signals will be examined. Extraction of pilot carriers is only possible if the transmitted signal is recovered at the receiver. In this research, a receiver synchronization algorithm for the opportunistic use of orthogonal frequency division multiplexing based Integrated Services Digital Broadcasting-Terrestrial (ISDB-T) digital television (DTV) signals in free-space has been developed. This synchronization algorithm can be developed further to account for the ionospheric effects on the ISDB-T DTV signals.

To

my beautiful wife, Mujde, who has supported my decisions under the most difficult situations, showed the true meaning of love, sacrifice, and togetherness, and repaired my wounds,

our beloved son, Arel, who gives joy to our lives for being so understanding to his daddy and being patient all the time,

and the loving memory of my father whom I will always miss...

ACKNOWLEDGMENTS

I would like to thank Prof. Kamalabadi for being my thesis adviser and expressing his support in me at all times. I learned a lot from him about research and how to develop methods towards successful research. Prof. William Robert Norris has opened a new door for me and introduced me to all the concepts surrounding autonomous vehicle systems class. Dr. Hasan Bahcivan provided the digital television signal data and gave his support and time for my research. Prof. Steven J. Franke allocated his time and shared his knowledge with me. He has also shown courtesy by being my thesis adviser and reviewing this thesis.

Leaving everything behind in our country, my wife and I sailed to a whole new experience. We were not only changing our location but also attaining new roles in our lives. Two one-way tickets for three! Starting a new life in a different country as a father- and mother-to-be and a parenting-graduate-student took some courage. We even had to object to and fight with the system a couple of times to get to where we have deserved to be. It would have been a much easier life if we had not pursued this adventure. But, thanks to our bold decisions, we grew up along with our baby boy, Arel. We always missed our parents, brothers, families and good friends that we had left behind, and today we still do. But, some other people we met were kind enough to assume these roles.

From the very first months in Champaign, Ilyas and Meral Kapan have always been like our parents and grandparents to our son. I have never met anybody so welcoming and uniting people around them. Their daughter, Selin Kapan, accepted us as her sister and brother and always showed her great love to our son. We have also made many friends in their joyful house on Green Street. They have also become good friends with our parents. They were available whenever we were in need. Sometimes we would drop by just to have

that familiar feeling of a cozy home we miss from times with our parents.

I was lucky enough to have come across some people who have been both mentors and friends to me. These people have made themselves available to me in my difficult times. Dr. Ruth Yontz not only helped me with one of the most challenging decisions of my life and job search, but also she reviewed and edited my thesis. Prof. Huseyin Sehitoglu helped me to understand the academic world. I am hoping to sail with him someday in the near future and continue our pleasant conversations. In the second half of my graduate education, I have become good friends with Dr. Cumali Aktolun and been counting myself fortunate to have great intellectual conversations with him.

Prof. Hüseyin Leblebici (R.I.P.) and Hakan Hatipoğlu introduced me to the business world and gave me the chance to discuss different aspects of this world. Prof. Hüseyin Leblebici and Dr. Ruth Yontz have always welcomed us with their always smiling faces, which fill hearts with happiness. Surely we miss Hüseyin Hoca every day. We started a lifelong friendship with Hakan. He found us our current home, became a good neighbor and a great friend. We spent so many hours talking on different topics and widening our understandings on them.

We had great friends here. It started with Çağdaş Tuna who welcomed us when we first came to Champaign. Then, we met Ayşegül, who turned out to be a classmate of my cousin from Moda Elementary School. Ayşegül and Serdar Aygün's hospitality is never forgotten. Figen Öktem, Gizem Gezer, Mikael Templeton, Deniz Ay, Aslıhan Karataş, Ergin Bulut, Güliz Seray Tuncay, Ozan Kahraman, Neriman Tokcan, and Renato Muncaso who taught me a lot about the C programming language have been with us in our good and bad times. Our good friends Gökhan Atınç and Giray Enkavi (Giray was also my roommate for a summer and had also been my neighbor in Istanbul) have always been around us and became an uncle to our son. Fabio Augusto Vargas has been one of my best friends and will remain a great friend all my life. He has always been there for me in good and bad times. I am so glad to see him happy with his beloved wife, Maria. We became great friends with Süreyya, Ebru Taşkan, and their son, Deniz. I hope we can fit more common memories in our lives. I know these friendships will last forever, and we will see good days

of our kids together.

Although we had challenging times in Champaign-Urbana, one can see that we were also very fortunate to have so many good people in our lives.

My mother, Hatice Ülfet Gezer, my father, Ersan Gezer (R.I.P.), and my brother Hüseyin Bülent Gezer, have helped me to elaborate on my thoughts and supported all my decisions. Their trust and love meant so much to me in my most difficult times. Loss of my father was the worst pain I have encountered in my life, and today I still carry this wound. I do and will miss him all the time.

My mother-in-law, Türkan Peksaygılı, and my father-in-law, Avni Peksaygılı, who have been like a father and mother to me, and my brother-in-law, Mutlu Peksaygılı, have always shown their support to me during my education. They never lost their trust in me. We know that they feel sorrow over being away from us but also welcome this situation with great empathy, respect, and understanding as they want the best for us. Türkan and my aunt, Nilgül Özbörek, stayed with us for many months and gave us the relief in times we needed most.

You might have noticed that I kept using "we" instead of "I". The reason is that my wife, Müjde Peksaygılı Gezer, and our son, Arel Bora Gezer, have been with me throughout this travel with lots of adventures. I am so happy to have fallen in love with and been married to this beautiful, smart and strong woman. Her patience, sacrifice, and understanding are beyond words. Being a parenting graduate student is very hard and maybe is a "continuous regret" as I heard from another parenting graduate student before. Our son has been so understanding of his dad's long work hours and listened to my reasons patiently. I could not imagine how such a little heart could make such a significant impact on my life before becoming a father. He has been the joy of our lives. I am truly sorry for the times I could not make available to my wife and our son and am hoping to make up for them.

I am happy to have added Chambana as one of the stations in our lives. Let's move to the next station and always enjoy the scene!

TABLE OF CONTENTS

LIST OF TABLES

LIST OF FIGURES

CHAPTER 1

INTRODUCTION

1.1 Motivation

Electromagnetic waves, acoustic waves, and magnetohydrodynamical waves propagate in different types of media like the atmosphere, ocean, and plasma. Waves always interact with the medium resulting in different phenomena such as diffraction, refraction, interference, and scattering. One of these phenomena is scintillations, which may result from regular or random inhomogeneities in the propagation medium.[1] Ionospheric scintillations, random changes in amplitude and phase of signals propagating through the turbulent ionosphere, are caused by the random fluctuations of electron density in the ionosphere, resulting in changes in refractive index [*Tatarskii et al.*, 1993].[2] Ionospheric scintillations vary with frequency, magnetic and solar activity, latitude, time of day, and season [*Jursa et al.*, 1985].

Satellite-based communication signals are profoundly affected by these scintillations. For GPS satellites, strong scintillations may cause the receiver to lose the signal, and weak scintillations can degrade accuracy. Many 2-D models have been developed for understanding ionospheric irregularities. *Huba et al.* [2008] and *Retterer* [2010] adopted a 2-D solution by incorporating equipotential field lines in a 3-D model. Aveiro and Hysell [2010; 2012] showed that a 2-D model was not sufficient to simulate the details of the physics of ionospheric F-region. However, using a 3-D ionospheric model, they could simulate

[1] As the other media and regular inhomogeneities are beyond the scope of this thesis, only random inhomogeneities in the ionospheric medium will be discussed.

[2] Refractive index, n is defined by $n = \sqrt{\epsilon_r}$, where ϵ_r, the relative permittivity is a function of electron density, N_e.

the first evolution of equatorial spread-F as well as bottom-type, bottomside, and topside stages. *Keskinen et al.* [1998] developed a quasi-three-dimensional model with magnetic flux tube integration techniques to demonstrate the nonlinear evolution of ESF bubbles. Later, *Keskinen et al.* [2003] found that parallel conductivity slows down both the linear and nonlinear bubble evolution. This effect was not observed with the 2-D evolution model. *Aveiro and Huba* [2013] presented a comparative study of the evolution of equatorial F-region irregularities using a 2-D and 3-D electrostatic potential solution in SAMI3 model. This comparison showed that the complex physics of the equatorial F region could be captured only by using a 3-D model.

Although *Hey et al.* [1946] brought scintillation to the attention of the scientific community by pointing out the short-period random fluctuations observed in radiations at 64 MHz from the radio star Cygnus, it was the deployment of Sputnik in 1957 that started a new era in scintillation studies. Since then, beacons carried by artificial satellites have proved to be a great asset. Recently, a new satellite named Ionospheric Scintillation Explorer (ISX) was developed by SRI International, Inc., and California Polytechnic State University and funded by the National Science Foundation.[3] [4] The nanosatellite's objective is to take measurements of the k-spectrum of equatorial spread-F (ESF) irregularities. These measurements will help us understand the scintillation-scale turbulence in and around the ESF plumes. Until now, experiments carried out by different missions to date could provide data for only the transverse (to the geomagnetic field) k-spectrum. However, ISX will also measure the parallel (to the geomagnetic field) k-spectrum, which is very valuable in understanding the three-dimensional electrodynamics of ESF turbulence [*Iuliano and Bahcivan*, 2015].

The ionosphere may be assumed to have inhomogeneities with an excess and deficient number of electrons which scatter waves randomly. ESF is known to obey universal power-law spectrum in the plane transverse to the geomagnetic field. One of the objectives of the ISX mission is to understand the spectrum of turbulence along a geomagnetic field

[3] In this thesis, *nanosatellite*, *Cubesat*, *mission*, and *spacecraft* will be used interchangably to refer to ISX.

[4] The satellite was deployed on December 15, 2018.

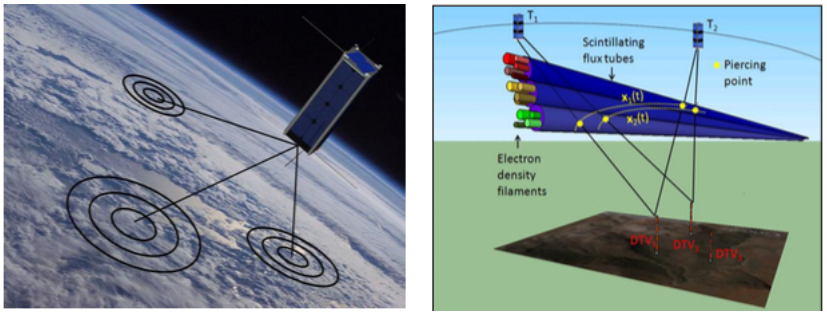

Figure 1.1 – (Left) Artist's rendering of the ISX cubesat receiving the DTV transmissions represented by concentric circles. (Right) A simulation of the experimental geometry is shown. Solid black lines show the line-of-sight between the transmitters and the satellite pierces through the magnetic flux tubes are represented in red. The trajectory of the satellite is represented with a black line between positions of the satellite denoted T_1 and T_2 [*Iuliano and Bahcivan*, 2015].

line. The k-parallel spectrum information will answer whether such a universal law is also valid in the parallel direction. The scintillation patterns at multiple transverse look angles will also show us if the irregularities causing scintillations are isotropic in the transverse plane. The data that will be collected by ISX will provide an excellent opportunity to evaluate the accuracy of the current models and improve them even further. Unlike most satellites deployed for research on scintillations, which carry a beacon, ISX is equipped with a four-channel UHF receiver which records the digital television signals broadcast by multiple ground transmitters. The signals pierce through the magnetic flux tubes at multiple points. Scintillations occur due to forward diffractive scattering of the signals of ESF irregularities. These scintillating signals are collected by the ISX receiver in near-real time [*Iuliano and Bahcivan*, 2015]. Figure 1.1 provides a representation of the experimental geometry.

With the opportunistic use of digital television (DTV) signals, the ISX mission brings a novel approach to the field, an approach that will complement the capabilities of other instruments such as incoherent scatter radars (ISR), rockets, sky camera, satellites, and GPS receivers, which are used to study ionospheric scintillations. ISR and sky cameras cannot detect scintillation-scale (100 m - 1000 m) irregularities. Although useful for observing meter scale regions, ISRs are expensive to operate. Sky cameras are used for large scales. Rockets or satellites cannot provide the needed spatial sampling of the magnetic flux tubes

as it is not easy to make them follow magnetic flux tubes [*Bahcivan and Novoselov*, 2016]. Although GPS receivers seem like a good alternative; due to the dispersive nature of the ionosphere, multi-frequency digital TV signals make a better asset to observe the internal consistencies in the models and theories developed [*Tatarskii et al.*, 1993].

The orbit of ISX is designed to capture the timely occurrence of ionospheric irregularities within F-layer (200-1000 km). For high and equatorial latitudes, the irregularities are observed predominantly in the ranges from 250 to 450 km. From time to time, E-layer irregularities can be observed at altitudes ranging from 90 to 100 km [*Jursa et al.*, 1985]. Globally, the intensity of scintillations in the auroral zone and the equatorial region is highest [*Aarons et al.*, 1971]. The equatorial region comprises the latitudes of ± 20 degrees around the magnetic equator. In the equatorial region, ionospheric irregularities almost always happen after sunset. ISX will make a circular orbit with an 85-degree inclination and will cross the magnetic equator around sunset. Its altitude will be at or above the ESF bubbles (250-500 km).

This research develops a receiver synchronization algorithm for Integrated Services Digital Broadcasting-Terrestrial (ISDB-T) DTV signals. As ISX orbits, its receiver payload will collect DTV signals and extract the pilot carriers from these signals. Cross-correlation of the phase and amplitude of these pilot carriers provides a useful tool for us to measure the spatial extent of the scintillating flux tubes [*Iuliano and Bahcivan*, 2015]. Disturbances added by the channel can make it challenging to perform the task of extracting pilot carriers from the received signal. Therefore, a receiver synchronization algorithm is needed to make sure the collected DTV signals have the same format as the transmitted signals.

1.2 Outline

This thesis is organized as follows. Chapter 2 provides a general introduction to orthogonal frequency division multiplexing (OFDM) as it is the modulation method used in ISDB-T systems. The chapter also provides general information on different types of digital broadcasting formats currently in use in different regions of the world. Chapter 2 concludes with a description of the structure of ISDB-T DTV signals. Chapter 3 provides

theoretical background on receiver synchronization. Chapter 4 applies this theoretical knowledge to develop a compact solution to receiver synchronization problem for ISDB-T DTV signals. Chapter 5 discusses the effectiveness of this research and proposes ideas for future work.

CHAPTER 2

ORTHOGONAL FREQUENCY DIVISION MULTIPLEXING AND ITS APPLICATION IN DIGITAL TELEVISION BROADCASTING SYSTEMS

2.1 Multi-carrier Transmission Schemes

Historically, television signals were broadcast with single-carrier transmission methods. Although these methods are simple to apply in flat fading channels, they require a high-complexity equalizer for frequency-selective channels. A typical equalizer is a finite impulse response filter with adaptive tap coefficients. Complexity arises from the fact that more taps are required for frequency-selective channels. Digital television broadcast requires a high-rate wireless transmission. This requirement brings two issues: inter-symbol interference (ISI) in the multi-path channels and need for a large signal bandwidth. As a high-complexity equalizer cannot be established in single-carrier schemes, multi-carrier schemes have been developed as an effective alternative.

In multi-carrier schemes, the frequency band is divided into subbands and multiple carriers are used for transmission. A filter bank of multiple narrow-band filters is found both at the transmitter and receiver structure, providing the ability to represent the frequency-selective wideband by multiple frequency-flat narrowband channels [*Cho et al.*, 2010]. This representation reduces the complexity of the equalizer for each subchannel (a.k.a. tone). Figure 2.1 shows the basic structure of a multicarrier system in which $X_\ell[k]$ and $Y_\ell[k]$ are the transmitted and received signals, respectively, at the carrier frequency f_k, $k = 0, 1, 2, ..., N-1$ and in the ℓ^{th} symbol interval. The panel at the bottom of the

figure shows that the whole wide bandwidth is divided into subbands of equal narrow bandwidths centered at subcarrier frequencies.[1] Table 4.1. in *Cho et al.* [2010] gives a compact comparison of single-carrier and multi-carrier transmission schemes.

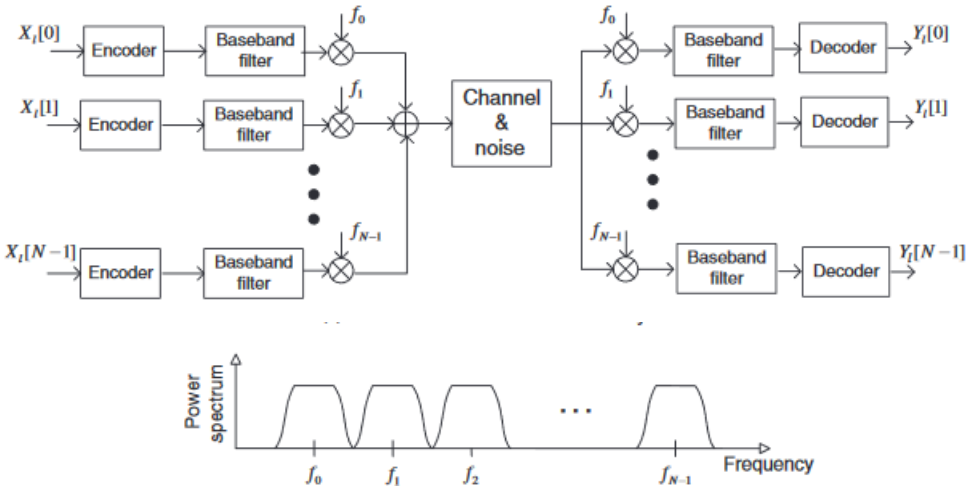

Figure 2.1 – The basic structure of a multicarrier transmission system is shown above while its spectral characteristics are shown below. If each subchannel in the lower panel is bandlimited, the system is called a filtered multi-tone (FMT) system. [*Cho et al.*, 2010].

Although multicarrier transmission systems look like a good alternative to single-carrier systems, some complexity also arises due to the increasing number of encoders, decoders, filters and oscillators. A method called orthogonal frequency division multiplexing (OFDM) will be discussed next as a good solution to reduce this complexity.

2.2 Orthogonal Frequency Division Multiplexing

The multicarrier transmission system discussed in Section 2.1 is one implementation of the frequency division multiple access (FDMA) method. OFDM, another type of multicarrier transmission scheme, does not use individual components as required for each subchannel shown in Figure 2.1. A smart design leading to the OFDM method not only reduces the number of components needed for a multicarrier transmission/ reception sys-

[1] Subcarrier is a term used to distinguish the set of frequencies f_k from the RF carrier frequency [*Haykin and Moher*, 2005]

tem but also increases the bandwidth efficiency.

Two important problems must be tackled to make sure that each transmitted symbol can be recovered accurately at the receiver: inter-symbol interference (ISI) and inter-carrier interference (ICI). ISI among subchannels can be prevented when the sampling of subcarrier signals is performed by satisfying the Nyquist criterion

$$g(nT) = \delta[n] = \begin{cases} 1, & n = 0 \\ 0, & n \neq 0 \end{cases} \Longleftrightarrow \sum_{i=-\infty}^{\infty} G\left(f - \frac{i}{T}\right),$$

where $\Longleftrightarrow$ denotes operation of Fourier transform of the function between time and frequency domains and $g(nT)$ is the impulse response of overall end-to-end system given as

$$g(nT) = g_T(nT) * h(nT) * g_R(nT) * h^{-1}(nT),$$

where $g_T(nT)$, $g_R(nT)$, and $h^{-1}(nT)$ denote the impulse response of the transmitter, receiver filter, and equalizer, respectively [*Cho et al.*, 2010].

Each subchannel contains a carrier which is digitally modulated. The allocation of subchannels close to one another can still create interference between the adjacent subcarriers. Therefore, an issue of inter-carrier interference may arise. Keeping the subcarriers orthogonal to one another is a solution to this potential issue. Given two time-limited complex exponential signals $e^{j2\pi f_k t}$and $e^{j2\pi f_i t}$, orthogonality of these two signals is satisfied if

$$\frac{1}{T_{sym}} \int_0^{T_{sym}} e^{j2\pi f_i t} \cdot (e^{j2\pi f_i t})^* = \begin{cases} 1, & k = i \\ 0, & k \neq i \end{cases} \tag{2.1}$$

where $f_i = i/T_{sym}$,$i = 0, 1, 2, ..., N-1$, and $f_k = k/T_{sym}$, $k = 0, 1, 2, ..., N-1$. Sampling these signals at $t = nT_s = nT_{sym}/N$, $n = 0, 1, 2, ..., N-1$, Equation (2.1) can be written

as

$$\frac{1}{N}\sum_{n=0}^{N-1} e^{j2\pi \frac{k}{T_{sym}} \frac{nT_{sym}}{N}} \cdot \left(e^{j2\pi \frac{i}{T_{sym}} \frac{nT_{sym}}{N}} \right)^* = \frac{1}{N}\sum_{n=0}^{N-1} e^{j2\pi(k-i)\frac{n}{N}}$$
$$= \begin{cases} 1, & k = i \\ 0, & k \neq i \end{cases}.$$

to express it in discrete-time domain [*Cho et al.*, 2010].

Unlike mutlicarrier systems, subchannels overlap in OFDM systems. However, using the orthogonality property, the spectrum of the OFDM signal is designed such that the peak of one carrier corresponds to the null of another as shown in Figure 2.2. Orthogonality along with sampling at the Nyquist rate provides a desirable modulation/demodulation scheme.

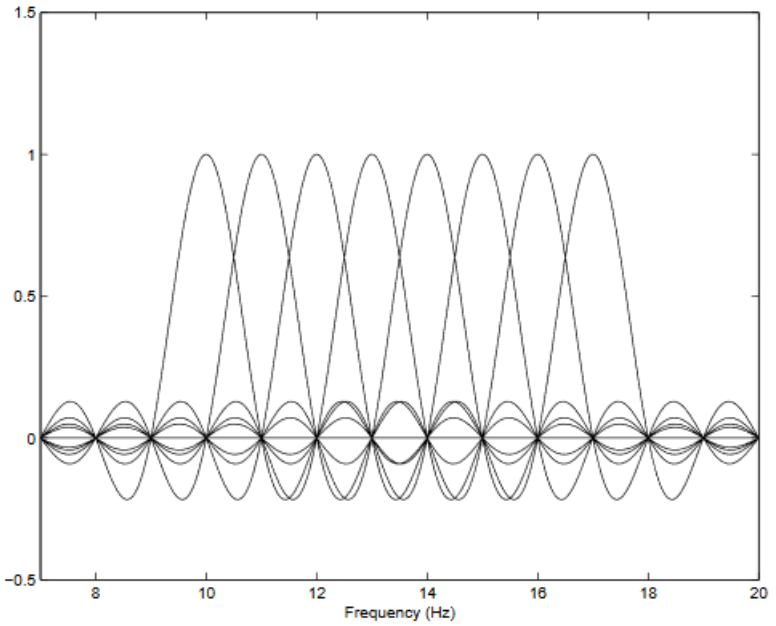

Figure 2.2 – Spectrum of OFDM signal with overlapping subcarriers [*Goldsmith*, 2005].

A general block diagram of an OFDM system is shown in Figure 2.3. Data bitstream is modulated by mapping into QAM or PSK modulation schemes. The serial modulated complex data bitstream in the frequency domain flows in N parallel streams, where N is the number of FFT points. During the serial-to-parallel conversion, pilot symbols are inserted

in the data to encode the information in amplitude variations [*Haykin and Moher*, 2005]. Within the duration of an OFDM symbol $T_{sym} = NT_s$, where T_s is the sampling period, ℓ^{th} OFDM transmit symbol in time domain is established after accumulating each subcarrier on which an IFFT operation is performed. To express this operation in mathematical terms, let $X_\ell[k]$ denote the ℓ^{th} transmit symbol at the k^{th} subcarrier, $\ell = 0, 1, ..., \infty$ and $k = 0, 1, ..., N-1$. Then, we can express the baseband OFDM signals

$$x_\ell(t) = \sum_{\ell=0}^{\infty} \sum_{k=0}^{N-1} X_\ell[k] e^{j2\pi f_k (t - \ell T_{sym})},$$

where $f_k = k/T_{sym}$. Sampling $x_\ell(t)$ at $t = \ell T_{sym} + nT_s$, a single discrete-time OFDM symbol becomes

$$x_\ell[n] = \sum_{k=0}^{N-1} X_\ell[k] e^{2\pi kn/N} \quad , n = 0, 1, ..., N-1$$

which is essentially N-point IDFT of the parallel data symbols [*Cho et al.*, 2010].

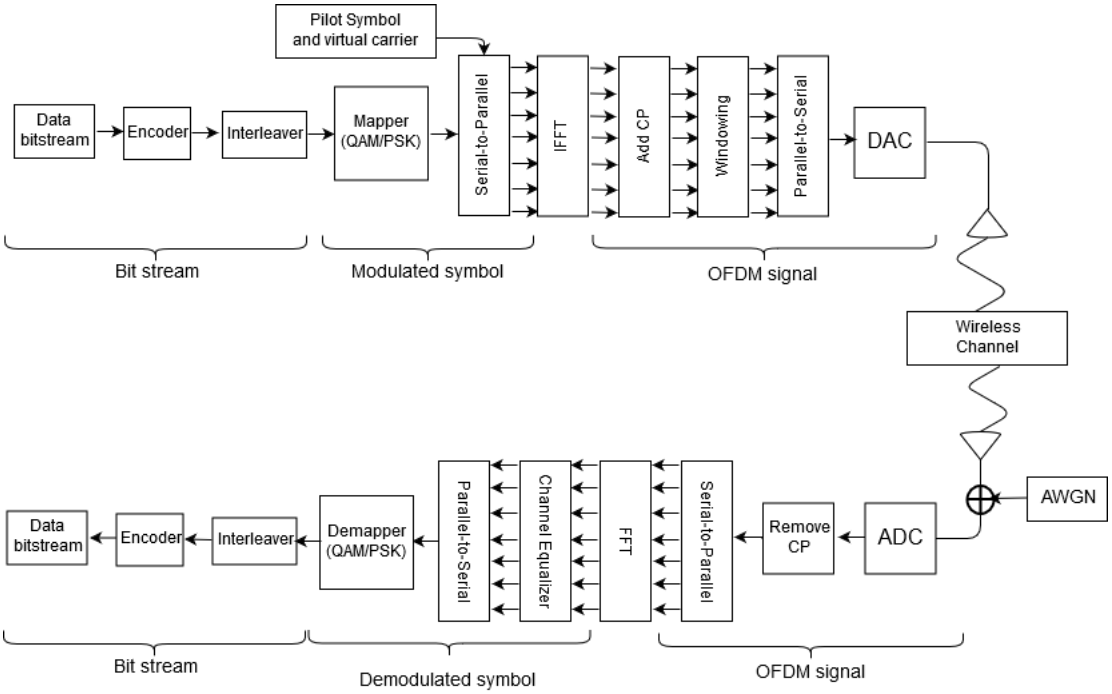

Figure 2.3 – Complete block diagram of an OFDM system [*Cho et al.*, 2010].

On the receiving end, from the received baseband signal in time domain

$$y_\ell(t) = \sum_{k=0}^{N-1} X_\ell[k] e^{j2\pi f_k(t-\ell T_{sym})}, \qquad \ell T_{sym} < t \leq (\ell+1)T_{sym},$$

using the orthogonality among the subcarriers in Equation (2.1), the transmitted symbol in frequency domain can be recovered with

$$\begin{aligned} Y_\ell[k] &= \frac{1}{T_{sym}} \int_{-\infty}^{\infty} y_\ell(t) e^{-j2\pi f_k(t-\ell T_{sym})}\, dt \\ &= \sum_{i=0}^{N-1} X_\ell[i] \left\{ \frac{1}{T_{sym}} \int_0^{T_{sym}} e^{j2\pi(f_i-f_k)(t-\ell T_{sym})} dt \right\} = X_{\ell[k]}, \end{aligned}$$

where the channel effects and noise are ignored [*Cho et al.*, 2010]. To perform FFT on the received OFDM symbol $y_\ell(t)$ we discretize it at $t = \ell T_{sym} + nT_s$

$$y_\ell[n] = \frac{1}{N} \sum_{i=0}^{N-1} X_\ell[i] e^{j2\pi in/N}$$

and take the FFT of the discrete OFDM symbol $y_\ell[n]$

$$\begin{aligned} Y_\ell[k] &= \sum_{n=0}^{N-1} y_\ell[n] e^{-j2\pi kn/N} \\ &= \frac{1}{N} \sum_{n=0}^{N-1} \sum_{i=0}^{N-1} X_\ell[i] e^{j2\pi(i-k)n/N} = X_\ell[k] \end{aligned}$$

Figure 2.4 shows an example of the OFDM modulation/ demodulation procedure for a symbol $X_\ell[k]$ modulating N subcarriers $k = 0, 1, .., 5$ with a frequency of $f_k = k/T_{sym}$.

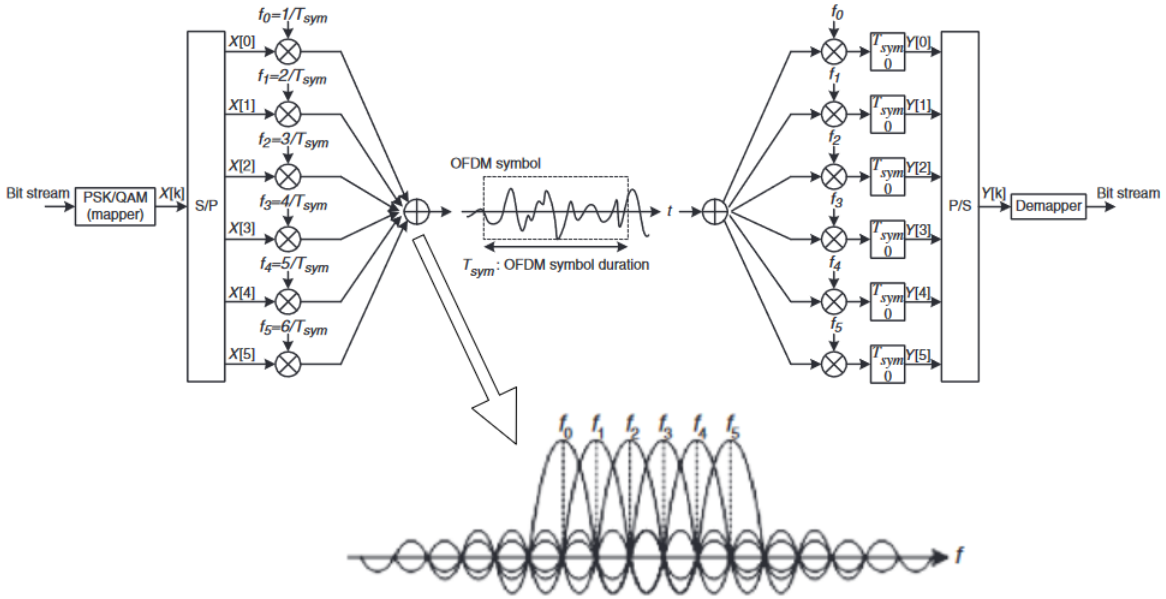

Figure 2.4 – Modulation and demodulation of OFDM symbols [*Cho et al.*, 2010].

Time-dispersive channels leads to ISI and the contiguous symbols are received as mixed with one another. In order to reduce the fading as a consequence of multi-path effects, a periodic interval is added to each OFDM symbol. This extension is called cyclic prefix (a.k.a. guard interval)[2] and its length should be longer than the estimated maximum delay of the multi-path channel to maintain the orthogonality among the subcarriers.

OFDM systems can be modeled as

$$Y_\ell[k] = X_\ell[k]H_\ell[k] + Z_\ell[k],$$

where, for the k^{th} subcarrier frequency component of the ℓ^{th} transmitted OFDM symbol, $H_\ell[k]$, and $Z_\ell[k]$ are the channel frequency response and noise in the frequency domain, respectively. Under no noise condition, $Z_\ell[k] = 0$, then the OFDM symbol can be detected by using a single-tap equalizer which can be described as

$$X_\ell[k] = \frac{Y_\ell[k]}{H_\ell[k]},$$

[2]In this work, GI and CP are used interchangeably.

which would be valid only if $X_\ell[k] \cdot H_\ell[k]$ was equal to the DFT of convolution of $x_\ell[n]$ with $h_\ell[n]$. However, $\text{DFT}\{x_\ell[n] * h_\ell[n]\} \neq X_\ell[k] \cdot H_\ell[k]$. Extending the OFDM symbol block in a cyclic manner allows the use of the circular convolution operator denoted $\otimes$. As a result, the cyclic prefix will make use of a single-tap equalizer for each subcarrier possible as $\text{DFT}\{x_\ell[n] \otimes h_\ell[n]\} \equiv X_\ell[k] \cdot H_\ell[k]$ [*Cho et al.*, 2010; *Goldsmith*, 2005].

Although the cyclic prefix has benefits, it also results in a data rate reduction of $N/(N + N_{CP})$, where N_{CP} is the length of the cyclic prefix. Also, some transmission power is wasted with the transmission of the cyclic prefix along with the OFDM symbol block. The cyclic prefix block can be zero-padded to save the related transmission power, but it does not improve the reduction of data rate [*Goldsmith*, 2005]. Cyclic prefix will be discussed more in its use in digital television signals and receiver synchronization in the rest of this thesis.

Efforts to develop a transmission scheme similar to OFDM go back to the 1950s [*Mosier and Clabaugh*, 1958; *van Nee and Prasad*, 2000]. This scheme found its use first in digital audio broadcasting and later in digital television broadcast applications. Due to the superiority of the OFDM transmission scheme, it has become the preferred system for many recent and current technologies.

OFDM is used in the modem standards ADSL and DOCSIS. It is also the scheme preferred in wireless LAN standards IEEE 802.11a/g/n/ac/ad as well as the WiMAX IEEE 802.16 set of standards. Wavelet-OFDM has evolved as an alternative to conventional OFDM used in power line communications due to its higher transmission efficiency and need for comparably fewer carriers [*Galli et al.*, 2008]. Already OFDM has a good performance in 4G and LTE technologies, and again a variation of OFDM called CP-OFDM has been selected as the waveform to be used in 5G technologies [*Zaidi et al.*, 2016], an ultra wideband (UWB) application. Multi-carrier UWB (MC-UWB) systems using OFDM have been developed as an alternative to impulse-UWB (I-UWB) systems. These systems are being studied for their possible implementation in ground penetrating radar and through-wall and medical imaging systems [*Reed*, 2005]. Levanon [2000a; 2000b] showed the application of OFDM in designing a multi-frequency radar signal. The autonomous ve-

hicle industry has created numerous innovations in sensing technology. Although FMCW is the radar waveform currently in use in this industry, possible ways of implementing UWB-OFDM/OFDM waveform in automotive radars are being investigated because of its robustness to multipath fading, multiple-use from its origin in communication systems, low sidelobes, almost no range-doppler coupling, and imaging capability [*Garmatyuk and Kauffman*, 2009; *Sit et al.*, 2011; *Sturm et al.*, 2009; *Sturm and Wiesbeck*, 2011].

2.3 Digital Terrestrial Television Broadcasting Standards

Digital television signals come in different formats depending on the country, frequency band and purpose of use. Due to the advantages they provide, digital video broadcasting systems have replaced analog television services. The main advantage is that digital television can provide multiple channels over a single stream using multiplexing. Another advantage is that digital video, audio and data broadcasting services can be provided via satellite, cable, or terrestrial signal delivery.

Different types of terrestrial digital television broadcast standards have developed around the world: Digital Video Broadcasting - Terrestrial (DVB-T), Advanced Television System Committer (ATSC), Integrated Service Digital Broadcasting - Terrestrial (ISDB-T), and Digital Terrestrial Multimedia Broadcasting (DTMB). Figure 2.5 shows the predominance of digital terrestrial television systems.

Digital Video Broadcasting - Terrestrial (DVB-T) is one of a series of standards adopted by the European Telecommunications Standard Institute. This series of standards define a set of principles for digital broadcasting of television, sound and data services . ISDB-T (Integrated Services Digital Broadcasting - Terrestrial), a digital broadcasting service, is a band-segmented transmission orthogonal frequency division multiplexing system. It provides audio, video and multimedia services. ISDB-TB is the Brazilian version of ISDB-T. ATSC (Advanced Television Systems Committee) is another set of digital broadcasting standards adopted by the United States, Canada, and South Korea. ATSC is the only type of digital broadcasting system using vestigial sideband modulation (VSB). DTMB (Digital Terrestrial Multimedia Broadcasting), previously known as DMB-T, was developed by the

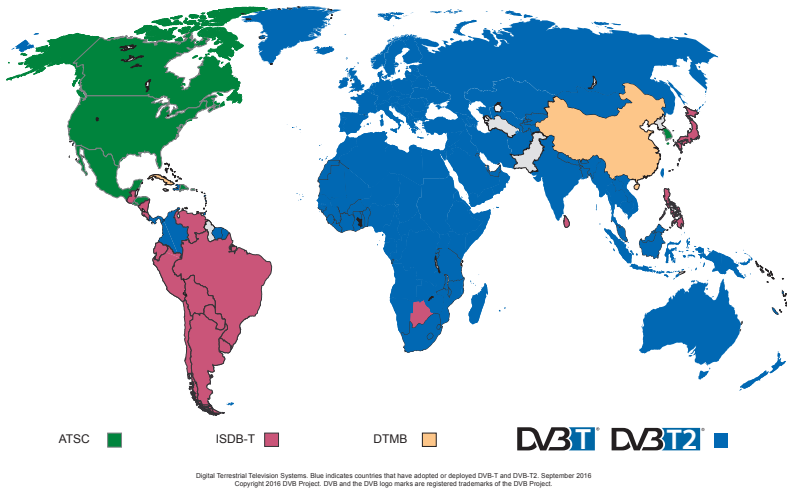

Figure 2.5 – Digital Terrestrial Television Systems around the World . DVB-T2 is the terrestrial version of second generation DVB (DVB-S2) that was adopted as a standard in 2014 [*DVB*, 2017].

People's Republic of China in 2004.

A brief comparison of these broadcasting services is provided in Table 2.1. Different types of orthogonal frequency division multiplexing techniques (OFDM) are in use. DVB-T uses Coded OFDM whereas DTMBS uses time-domain synchronization OFDM (TDS-OFDM). ISDB-T, on the other hand, which will be discussed next uses band segmented transmission-OFDM (BST-OFDM).

Table 2.1 – A comparison of broadcasting services.

	DVB-T	ATSC	ISDB-T	DTMB
Bandwidth	6/ 7/ 8 MHz	6 MHz	6/ 7/ 8 MHz	6/ 7/ 8 MHz
Modulation	COFDM	VSB	BST-OFDM	TDS-OFDM

2.4 Integrated Services Digital Broadcasting - Terrestrial Digital Television Signals

Sample data provided by SRI International was recorded from DTV stations in Brazil broadcasting in the ISDB-T format. The ISDB-T system operates on the BST-OFDM method. ISDB-T has three different modes based on spacings between OFDM carrier

frequencies. These spacings are approximately 4 kHz, 2 kHz, and 1 kHz in modes 1, 2, and 3, respectively.[3] Although the number of carriers is different for each mode, data bit rate remains the same in all modes. Modes 1, 2, and 3 have a bandwidth of 6, 7, and 8 MHz, respectively. The feature of different modes provides immunity of the signals to multipath propagation and Doppler effects.

By combining data carriers with control signal carriers we obtain OFDM segment which occupies $1/14$ of 6 MHz television channel bandwidth. In ISDB-T systems, transmission band consists of 13 subbands called OFDM segments. So, each OFDM segment has a bandwidth of $6/14 \approx 428.57$ kHz . OFDM frame consists of 204 OFDM symbols. Table 2.2 gives detailed information about each mode. Depending on the mode of transmission one OFDM symbol consists of 2^{11}, 2^{12}, or 2^{13} carriers which determine the number of FFT points. However, 108, 216, and 432 carriers per segment for each transmission mode results in allocation of 1405, 2809, and 5617 carriers per symbol for mode 1, 2, and 3, respectively.[4] This difference in the number of carriers in theory and practice arises from the fact that these carriers are enough to meet the bit-rate and bandwidth requirements [*Larroca et al.*, 2016]. Table 2.3 shows how many of those carriers are allocated for different purposes.

The orthogonality property of BST-OFDM allows simultaneous transmission of multiple sub-carriers within a limited bandwidth without interference. Orthogonality is established by setting the subband carriers at the harmonics of the carrier with the smallest frequency. Therefore, as seen in Figure 2.4, the spectrum of an OFDM signal is the sum of frequency shifted sinc functions. Having all sub-carriers with a finite duration T, these overlapped sinc functions are separated by $1/T$. Each sub-carrier acts like an independent channel due to the orthogonality property.

BST-OFDM is designed to have $1/4, 1/8, 1/16, 1/32$ of the symbol duration copied and allocated as guard interval (GI). Thus, a guard interval is located between two consecutive symbols. This structure is shown in Figure 2.6. A full time-frequency domain of OFDM

[3] For more precise information, see Table 2.3.

[4] Number of carriers per symbol is calculated using $N_s \times N_c + 1$ where N_s is number of subbands, i.e. 13 and N_c sumber of carriers per segment as shown in Table 2.3.

symbols and guard intervals is depicted in Figure 2.7. The combination of guard interval and data within one OFDM symbol is shown in Table 2.4.

An OFDM signal consists of a number of different carriers. An ISDB-T signal consists of the carriers of data, scattered pilot (SP), transmission and multiplexing configuration control (TMCC), and auxiliary channel (AC). Pilot carriers are added to the signal together with TMCC carriers before IFFT operation. Guard interval is added after IFFT is performed on the signal. These carriers are allocated within OFDM-segment.

Configuration of an OFDM segment for synchronous modulation, i.e. QPSK, 16QAM, and 64QAM is shown in Figure 2.8. As stated earlier, this OFDM-segment has 204 OFDM-symbols each of which is composed of 96 OFDM-carriers for Mode-1, 192 for Mode-2, and 384 for Mode-3. Each segment occupies $1/14$ of the total bandwidth which is $6000/14$ kHz $\approx$ 428.57 kHz. The scattered pilot carriers are distributed within this segment in a certain order.[5] Starting with the upper left corner of the segment, a scattered pilot is inserted once every 12 carriers and once every 4 symbols in carrier and symbol directions, respectively. A varying number of TMCC and AC carriers with the transmission mode are also allocated within the segment. These carriers are fixed in certain locations given in *ARIB STD-B31* [2005]. Pilot carriers are used for synchronization and reproduction purposes.

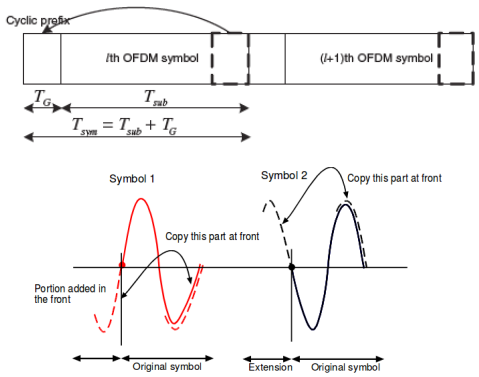

Figure 2.6 – Guard interval allocation. Guard interval is located between two consecutive symbols. Symbol duration is shared by subchannel and guard interval. The top panel is a block representation of the bottom one [*Cho et al.*, 2010; *Langton*, 2004].

[5] There are two types of pilots: scattered and continuous. Continuous pilots are used in differential modulation. ISDB-T signals have only one continuous pilot and it is located in the biggest carrier [*Larroca et al.*, 2016].

Table 2.2 – ISDB-T OFDM-segment parameters as shown in *ARIB STD-B31* [2005] by the Association of Radio Industries and Businesses (ARIB).

Mode		Mode 1		Mode 2		Mode 3	
Bandwidth		3000/7 = 428.57··· kHz					
Spacing between carrier frequencies		250/63 = 3.968··· kHz		125/63 = 1.9841··· kHz		125/126 = 0.99206··· kHz	
Number of carriers	Total count	108	108	216	216	432	432
	Data	96	96	192	192	384	384
	SP*1	9	0	18	0	36	0
	CP*1	0	1	0	1	0	1
	TMCC*2	1	5	2	10	4	20
	AC1*3	2	2	4	4	8	8
	AC2*3	0	4	0	9	0	19
Carrier modulation scheme		QPSK 16QAM 64QAM	DQPSK	QPSK 16QAM 64QAM	DQPSK	QPSK 16QAM 64QAM	DQPSK
Symbols per frame		204					
Effective symbol length		252 µs		504 µs		1008 µs	
Guard interval		63 µs (1/4), 31.5 µs (1/8), 15.75 µs (1/16), 7.875 µs (1/32)		126 µs (1/4), 63 µs (1/8), 31.5 µs (1/16), 15.75 µs (1/32)		252 µs (1/4), 126 µs (1/8), 63 µs (1/16), 31.5 µs (1/32)	
Frame length		64.26 ms (1/4), 57.834 ms (1/8), 54.621 ms (1/16), 53.0145 ms (1/32)		128.52 ms (1/4), 115.668 ms (1/8), 109.242 ms (1/16), 106.029 ms (1/32)		257.04 ms (1/4), 231.336 ms (1/8), 218.484 ms (1/16), 212.058 ms (1/32)	
IFFT sampling frequency		512/63 = 8.12698··· MHz					
Inner code		Convolutional code (1/2, 2/3, 3/4, 5/6, 7/8)					
Outer code		RS (204,188)					

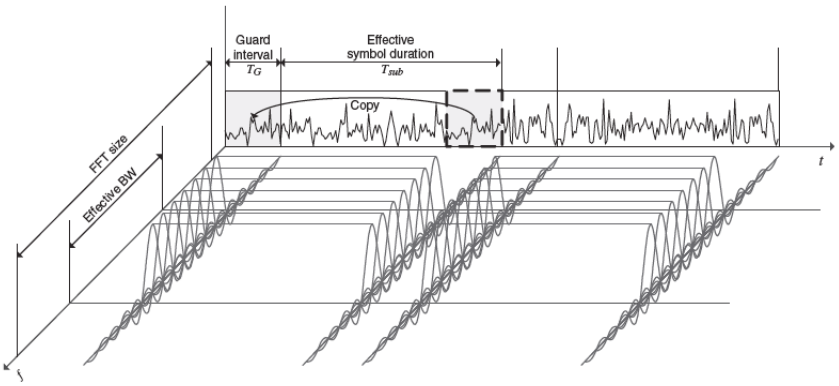

Figure 2.7 – OFDM symbols and guard intervals are shown in time and frequency domains [*Cho et al.*, 2010].

Table 2.3 – ISDB-T OFDM-transmission parameters as shown in *ARIB STD-B31* [2005] by the Association of Radio Industries and Businesses (ARIB).

Mode		Mode 1	Mode 2	Mode 3
Number of OFDM segments Ns		13		
Bandwidth		3000/7 (kHz) × N_s + 250/63 (kHz) = 5.575···MHz	3000/7 (kHz) × N_s + 125/63 (kHz) = 5.573···MHz	3000/7 (kHz) × N_s + 125/126 (kHz) = 5.572···MHz
Number of segments of differential modulations		n_d		
Number of segments of synchronous modulations		n_s ($n_s + n_d = N_s$)		
Spacings between carrier frequencies		250/63 = 3.968···kHz	125/63 = 1.984···kHz	125/126 = 0.992···kHz
Number of carriers	Total count	108 × N_s + 1 = 1405	216 × N_s + 1 = 2809	432 × N_s + 1 = 5617
	Data	96 × N_s = 1248	192 × N_s = 2496	384 × N_s = 4992
	SP	9 × n_s	18 × n_s	36 × n_s
	CP*1	n_d + 1	n_d + 1	n_d + 1
	TMCC	n_s + 5 × n_d	2 × n_s + 10 × n_d	4 × n_s + 20 × n_d
	AC1	2 × N_s = 26	4 × N_s = 52	8 × N_s = 104
	AC2	4 × n_d	9 × n_d	19 × n_d
Carrier modulation scheme		QPSK, 16QAM, 64QAM, DQPSK		
Symbols per frame		204		
Effective symbol length		252 μs	504 μs	1.008 ms
Guard interval		63 μs (1/4), 31.5 μs (1/8), 15.75 μs (1/16), 7.875 μs (1/32)	126 μs (1/4), 63 μs (1/8), 31.5 μs (1/16), 15.75 μs (1/32)	252 μs (1/4), 126 μs (1/8), 63 μs (1/16), 31.5 μs (1/32)
Frame length		64.26 ms (1/4), 57.834 ms (1/8), 54.621 ms (1/16), 53.0145 ms (1/32)	128.52 ms (1/4), 115.668 ms (1/8), 109.242 ms (1/16), 106.029 ms (1/32)	257.04 ms (1/4), 231.336 ms (1/8), 218.484 ms (1/16), 212.058 ms (1/32)
Inner code		Convolutional code (1/2, 2/3, 3/4, 5/6, 7/8)		
Outer code		RS (204,188)		

*1: The number of CPs represents the sum of those CPs in segments, plus one CP added to the right of the entire bandwidth.

Table 2.4 – Different combinations of N_{FFT}-N_G. In the table, N_{FFT} is the number of FFT points, N_G is the number of data points for guard interval and N_G/N_{FFT} is the guard interval ratio.

	Mode 1	Mode 2	Mode 3
N_{FFT}	2048	4096	8192
N_G/N_{FFT}	$1/4, 1/8, 1/16, 1/32$	$1/4, 1/8, 1/16, 1/32$	$1/4, 1/8, 1/16, 1/32$
N_G	$512, 256, 128, 64$	$1024, 512, 256, 128$	$2048, 1024, 512, 256$

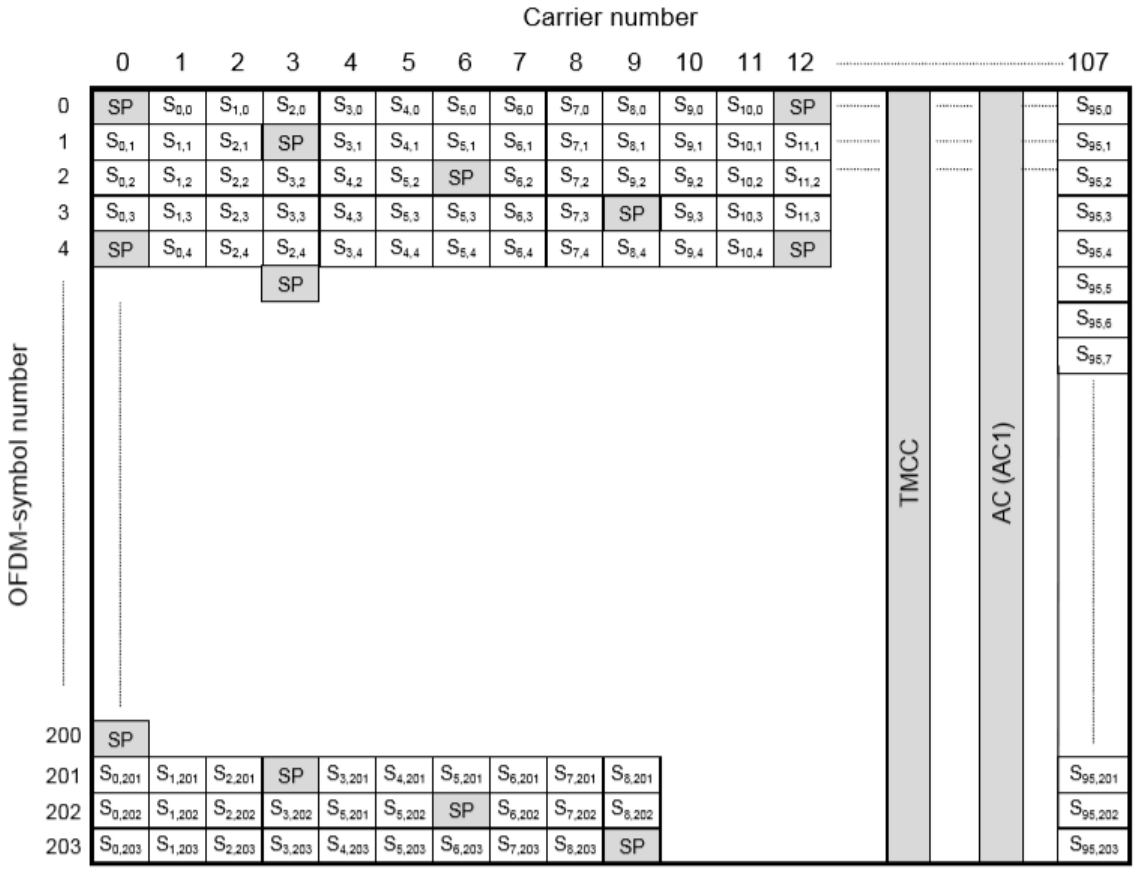

Figure 2.8 – OFDM segment configuration of an ISDB-T Mode 1 signal for synchronous modulation [*ARIB STD-B31*, 2005].

CHAPTER 3

SYNCHRONIZATION FOR ORTHOGONAL FREQUENCY DIVISION MULTIPLEXING BASED SYSTEMS

3.1 Overview

A transmitter modulates the bitstream into symbols on a modulation scheme, e.g., PSK, QAM. An IFFT operation is performed on these symbols. These symbols, which are transformed to time domain, are relayed through the channel. However, the channel distorts the signal and ultimately may remove the orthogonality of the OFDM signal. Therefore, the distortion needs to be compensated for at the receiver. This compensation can be accomplished through synchronization, which provides an accurate mapping of the symbols on the scheme, thereby properly performing demodulation of the OFDM signal.

OFDM synchronization is known to be a challenging task [*Larroca et al.*, 2016; *Cho et al.*, 2010; *Goldsmith*, 2005; *Pollet et al.*, 1995]. It mainly consists of the steps of estimation and correction of symbol timing offset (STO), carrier frequency offset (CFO) (also known as integer CFO) and sampling clock offset (SCO) [*Cho et al.*, 2010; *Larroca et al.*, 2016]. This chapter discusses these offsets and their effects on the received OFDM signals.

3.2 Symbol Timing Offset

In order to adjust symbol timing offset, the starting point of each OFDM symbol after the GI is removed must be determined. This determination provides symbol timing for properly performing an FFT operation in the receiver. In the time domain, the effect of

STO in the received signal can be expressed as

$$y_\ell[n] = x_\ell[n+\theta].$$

For a representation in the frequency domain, the FFT of the time domain received signal is taken

$$Y_\ell[k] = \frac{1}{N}\sum_{n=0}^{N-1} x_\ell[n+\theta]e^{-j2\pi nk/N}, \tag{3.1}$$

where the transmitted signal can be expressed as

$$x_\ell[n+\theta] = \sum_{p=0}^{N-1} X_\ell[p]e^{j2\pi(n+\theta)p/N},$$

and thereby Equation (3.1) yields

$$\begin{aligned} Y_\ell[k] &= \frac{1}{N}\sum_{p=0}^{N-1} X_\ell[p]e^{j2\pi\theta/N}\sum_{n=0}^{N-1} e^{j2\pi\frac{(p-k)}{N}n} \\ &= X_\ell[k]e^{j2\pi k\theta/N}, \end{aligned}$$

after using the following identity

$$\begin{aligned} \sum_{n=0}^{N-1} e^{j2\pi\frac{(p-k)}{N}n} &= e^{j\pi(p-k)\frac{N-1}{N}}\cdot\frac{\sin[\pi(k-p)]}{\sin[\pi(k-p)/N]} \\ &= \begin{cases} N & \text{for k=p} \\ 0 & \text{for k}\neq\text{p} \end{cases}. \end{aligned}$$

In the above set of equations ℓ is the symbol number, k is the subcarrier index and N is the number of points for FFT [*Cho et al.*, 2010]. These equations show that timing offset causes a phase rotation in the received signal. If the estimated point corresponds to somewhere within the symbol, then both inter-carrier interference (ICI) and inter-symbol interference (ISI) can be seen.

3.3 Carrier Frequency Offset

Carrier frequency offset results from Doppler frequency shift, timing synchronization errors and a mismatch between the local oscillator frequencies at the transmitter and receiver. The passband signal which was converted from the baseband signal during modulation is converted back to baseband by mixing it with a local carrier signal. The frequencies of the local oscillators at the transmitter and receiver must be the same. Otherwise, a carrier frequency offset occurs, which causes a missmatch, $\Delta\phi = \phi_r - \phi_t \neq 0$, between the carrier phase ϕ_r at the receiver and the carrier phase ϕ_t at the transmitter . Carrier frequency recovery as well as timing recovery takes place prior to the demodulation step.

In a general sense, normalized CFO denoted ϵ is a ratio given by

$$\epsilon = \frac{f_{offset}}{\Delta f},$$

where f_{offset} is the difference between the carrier frequencies at the transmitter and receiver and Δf is the subcarrier spacing [*Cho et al.*, 2010]. The received signal involving the effects of CFO can be expressed as

$$y[n] = x[n]e^{j2\pi n\epsilon/N}$$

in time domain, and

$$Y[k] = X[k - \epsilon]$$

in frequency domain. This shift in frequency domain may cause an ICI as shown in Figure 3.1.

CFO is basically composed of two parts, $\epsilon = \epsilon_I + \epsilon_f$, where ϵ_I is the integer CFO and ϵ_f is the fractional CFO. Integer CFO shifts the transmitted signal $X[k]$ in a cyclic manner. Therefore, the input of FFT is $x[n]e^{j2\pi\epsilon_I n/N} \longleftrightarrow X[k-\epsilon_I]$ for the k^{th} subcarrier. Although this kind of offset degrades the bit error rate (BER) greatly, orthogonality among subcarriers is maintained, and thus no ICI is of concern. However, every subcarrier is found at the wrong position. Fractional CFO, on the other hand, causes the loss of orthogonality

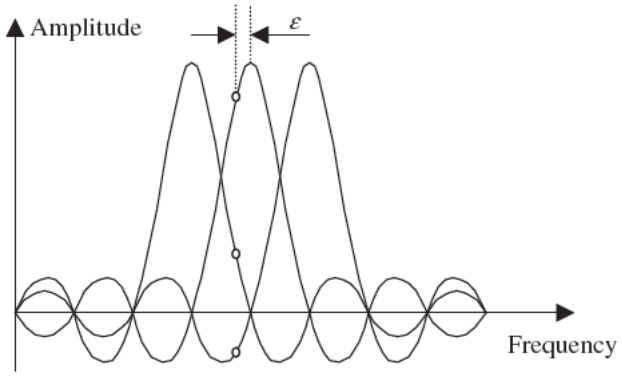

Figure 3.1 – CFOcauses an inter-carrier interference [*Cho et al.*, 2010].

among the subcarriers and increases the bit error rate (BER) [*Liu et al.*, 2004; *Pollet et al.*, 1995].

To show the effect of fractional CFO on the received signal $y[n]$, an FFT operation is performed

$$Y[k] = \sum_{n=0}^{N-1} y[n] e^{-j2\pi kn/N}.$$

The received signal in time domain before FFT is given by

$$y_\ell[n] = \frac{1}{N} \sum_{k=0}^{N-1} H[k] X_\ell[k] e^{j2\pi(k+\epsilon_f)n/N} + w_\ell[n], \tag{3.2}$$

where $w[n]$ denotes the noise, and $H[k]$ represents the channel response. Then, the received signal in frequency domain becomes

$$Y_\ell[k] = H_\ell[k] X_\ell[k] \frac{\sin(\pi\epsilon_f)}{N \sin(\pi\epsilon_f/N)} \cdot e^{j\pi\epsilon_f(N-1)/N} + I_\ell[k] + W_\ell[k],$$

where

$$I_\ell[k] = e^{j\pi\epsilon_f(N-1)/N} \sum_{m=0, m\neq k}^{N-1} H[m] X[m] \frac{\sin(\pi(m-k+\epsilon_f))}{N \sin(\pi(m-k+\epsilon_f)/N)} e^{j\pi(m-k)(N-1)/N}$$

represents ICI and the first term represents the amplitude and phase distortion of the kth subcarrier frequency component due to the fractional CFO [*Cho et al.*, 2010; *Muschallik*, 1995].

3.4 Sampling Clock Offset

SCO consists of phase offset and frequency offset in the sampling clocks. Frequency offset results from a frequency mismatch between the local oscillators at the transmitter and receiver or Doppler frequency, and phase offset corresponds to the non-identical sampling rates at the transmitter and receiver which causes a symbol timing error [*Yang et al.*, 2000a; *Speth et al.*, 1998]. Figure 3.2 distinguishes between the frequency and phase offsets resulting from SCO.

While CFO is the same for all subcarrriers, SCO contributes linearly with the subcarrier index, which can be expressed in a block of N_{sub} subcarriers as

$$\Delta f = \Delta f_c + k \cdot \Delta f_s, -\frac{N_{sub}}{2} \leq k < \frac{N_{sub}}{2},$$

where Δf_c is the carrier frequency offset, Δf_s is the sampling frequency offset, and k is the subcarrier index [*Sandell et al.*, 2005]. SCO due to the phase offset is proportional to the timing offset and subcarrier index and evaluated as a very small part of STO. Therefore, it is often neglected [*Cho et al.*, 2010]. Sampling clock frequency offset is given by

$$\zeta = \frac{(f_{s_{TX}} - f_{s_{RX}})}{f_{s_{TX}}},$$

where $f_{s_{TX}}$ and $f_{s_{RX}}$ are the sampling frequencies at the transmitter and receiver, respectively [*Fechtel*, 2000; *Pollet et al.*, 1994, 1995].

3.5 Total Offset

Different types of offsets have been discussed in this chapter. A general review of their effects on the received signal is shown in Table 3.1.

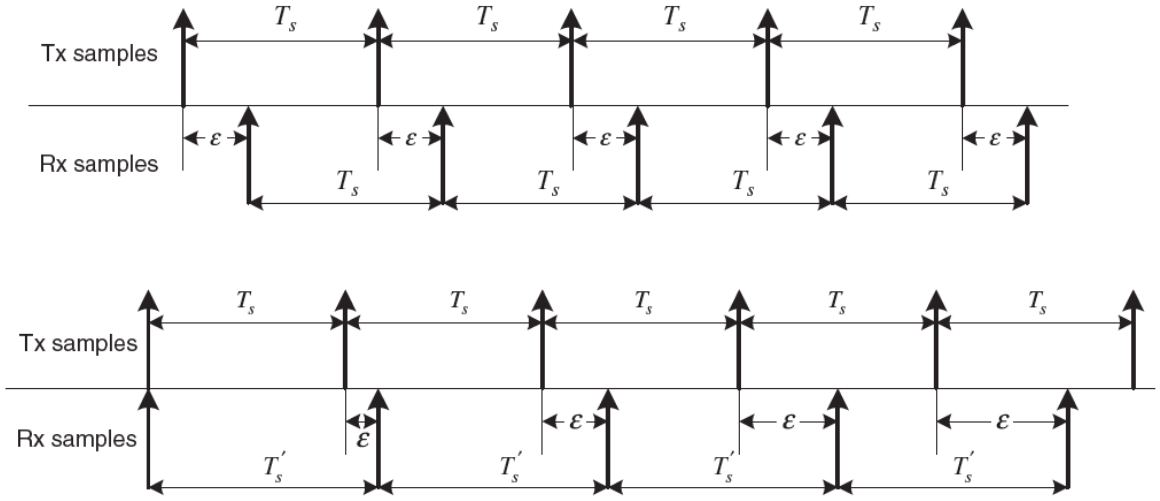

Figure 3.2 – Phase and frequency offsets in *SCO*. The top panel shows the constant time difference between Tx and Rx samples due to phase offset. The bottom panel shows that SFO causes a time-varying phase offset in clocks, which causes inter-carrier interference [*Cho et al.*, 2010].

Table 3.1 – The effect of the offsets on the received signals in the time and frequency domains.

	Time domain	Frequency domain
STO	$y[n] = x[n+\theta]$	$Y[k] = X[k]e^{j2\pi k\theta/N}$
CFO	$y[n] = x[n]e^{j2\pi n\epsilon/N}$	$Y[k] = X[k-\epsilon]$
SCO	$y[n] = x[n+\zeta]$	$Y[k] = X[k]e^{j2\pi k\zeta/N}$

The total effect of *STO*, *CFO* and *SCO* in the received baseband signal can be shown as

$$\begin{aligned} y_\ell[n] &= IDFT\{Y_\ell[k]\} \\ &= IDFT\{H_\ell[k]X_\ell[k] + Z_\ell[k]\} \\ &= \frac{1}{N}\sum_{k=0}^{N-1} H_\ell[k]X_\ell[k]e^{j2\pi(k+\epsilon)(n+\theta+\zeta)/N} + z_\ell[n], \end{aligned}$$

where $\epsilon = \epsilon_I + \epsilon_f$. Chapter 4 explains how the errors mentioned above are estimated and the pilot carriers are extracted from the received signal.

CHAPTER 4

APPLICATION OF A FULL RECEIVER SYNCHRONIZATION METHOD TO OFDM-BASED ISDB-T DTV SIGNALS

4.1 Overview

The block diagram in Figure 4.1 shows the steps of ISDB-T receiver synchronization developed for this research. This chapter discusses the estimation of symbol timing offset, carrier frequency offset, sampling clock and finally extraction of pilot carriers. The chapter concludes with demonstration of how these estimation procedures are applied to the data recorded from an ISDB-T broadcast station.

4.2 Data Preparation and Mode Estimation

The ETTUS receiver which was used to record the ISDB-T broadcast signals has a constant resampling rate of 8 MHz. As DTV signals are always transmitted at 8.12698... MHz a rational resampling is done at a rate of $64/63$. Data is stored in blocks. Each block data has $1,048,576$ sample points. Number of sample points increases to approximately $1,065,220$ after resampling the data.

Resampling operation was done by using the resampling tool that was developed by David Cournapeau. Considering that it is written in a low-level language, this tool performs the cumbersome resampling process in a relatively small period of time.[1]

[1]The package can be accessed at pypi.org's website (Access date : 05/10/2019). This is a Python wrapper around the algorithm written in C programming language by Eric de Castro Lopo based on *Putnam and Smith* [1997].

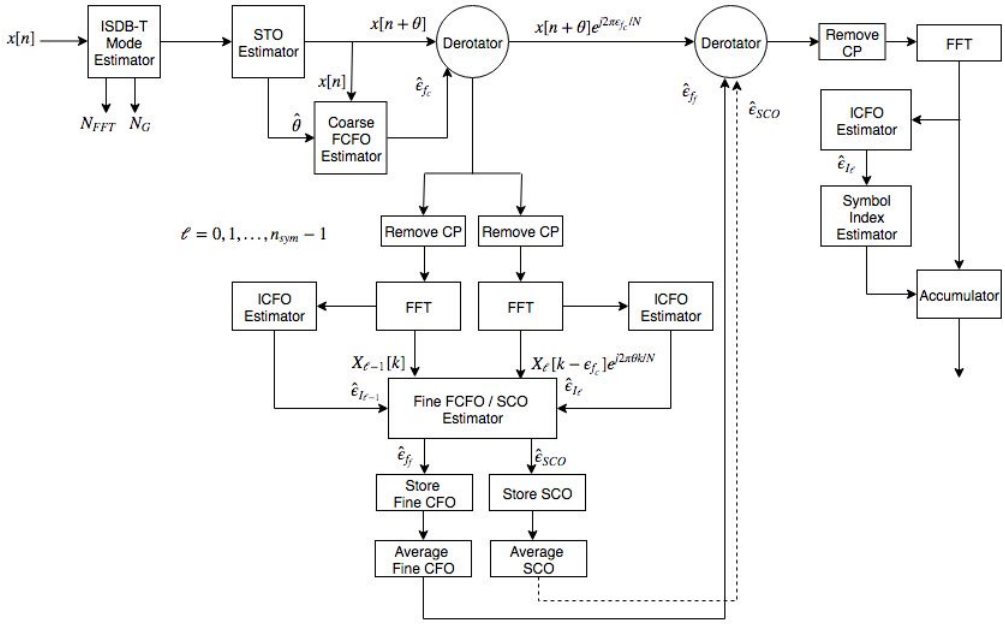

Figure 4.1 – Receiver synchronization of ISDB-T OFDM signals. To keep the diagram simple, the block showing the function generating pseudo-random bit sequence (PRBS) is not shown.

As data is composed of OFDM symbols it is vital to determine the length of the symbol and the GI ratio. N_{FFT} is estimated to determine the ISDB-T mode. The resampled data is scanned for all possible pairs of N_{FFT} and N_G lengths listed in Table 2.4. For different lengths, different numbers of symbols are found since

$$n_{sym} = \frac{N}{N_{FFT} + N_G},$$

where N is the number of samples in the whole set of data after resampling. To determine the correct pair of $N_{FFT} - N_G$ the auto-correlation of the received signal is checked

$$\arg \max_{N_{FFT}, N_G} \left\{ \sum_{i=0}^{N_{FFT}+N_G-1} \sum_{\ell=0}^{n_{sym}-1} y_\ell[i + \ell \cdot (N_{FFT} + N_G)] y_\ell^*[i + \ell \cdot (N_{FFT} + N_G) + N_{FFT}] \right\},$$

and correlation is found to be maximum at $N_{FFT} = 8192$ and $N_G = 2048$ for the data analyzed in this research.

4.3 Estimation of Symbol Timing Offset

Due to the channel delay θ, the position of the symbol in the received signal is not known. It is important to find the exact starting point of a symbol to compensate for STO, which is estimated in time domain by using the GI.

STO should be located somewhere along the GI and OFDM symbol. Because GI is a portion copied from the OFDM symbol, GI is useful in estimating STO. As shown in Figure 4.2, two blocks of N_G samples are created and slid along the OFDM symbols by checking the correlation between the windows. A maximum likelihood technique is applied to determine the location at which the correlation is maximized, as given by

$$r_{xx}(\theta, \theta + N_{FFTT}) = \sum_{\theta=0}^{N_{FFT}+N_G-1} \sum_{\ell=0}^{n_{sym}-1} x[\theta + \ell \cdot (N_{FFT} + N_{CP})] \cdot x^*[(\theta + N_{FFT}) + \ell \cdot (N_{FFT} + N_{CP})],$$

where $x[n] = I[n] + jQ[n]$. The auto-correlated signal is passed through a matched filter in order to estimate the symbol timing offset

$$\hat{\theta} = \arg\max_{\theta} \left\{ \sum_{\theta=1}^{N_{FFT}} r_{xx}[\theta - 1 + N_{CP}] - r_{xx}[\theta - 1] + \sum_{\theta=N_{FFT}+1}^{N_{FFT}+N_{CP}} r_{xx}[\theta - 1 - N_{FFT}] - r_{xx}[\theta - 1] \right\}. \quad (4.1)$$

Note that estimation of STO is made in the time domain before the received signal is demodulated. When Equation (4.1) yields maximum, guard interval of an OFDM symbol meets the first sliding window. The estimation of θ does not change from symbol to symbol. However, synchronization may be lost because the receiver skips some samples to record [*Larroca et al.*, 2016].

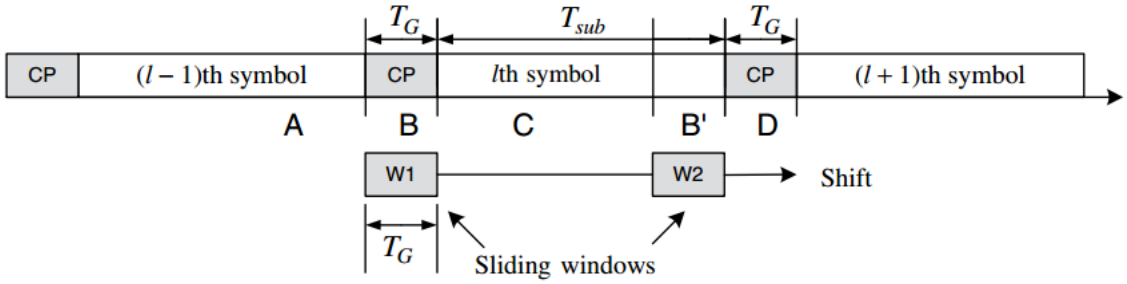

Figure 4.2 – Estimation of STO by using double windows slid along the OFDM symbols. The first window of N_G samples reside in B whereas the second window of the same length is located in $B^{'}$. These two blocks are separated N_{sub} samples over T_{sub} which corresponds to the effective data. [*Cho et al.*, 2010]

4.4 Estimation of Carrier Frequency Offset

As mentioned in Section 3.3, CFO is composed of two parts : integer CFO ($ICFO$) and fractional CFO ($FCFO$), namely $\epsilon = \epsilon_I + \epsilon_f$. The fractional part is estimated using two steps: acquisition and tracking. [2] In the acquisition step, one estimate in time domain at the very first symbol is made and, using the guard interval , a coarse $FCFO$ is obtained

$$\hat{\epsilon}_{f_c} = \frac{1}{2\pi} \arg \left\{ \sum_{n=0}^{N_G-1} |y_\ell[\theta+n] y_\ell^*[\theta+n+N_{FFT}]| \right\}, \tag{4.2}$$

where $\ell = 0$, and the subscipt c denotes the estimation being coarse. Function $atan2$ is used for the arg operator in Equation (4.2). Averaging is applied to reduce the noise effects [*Cho et al.*, 2010]

Due to CFO, the phase of the signal at the receiver is rotated by $2\pi n\epsilon/N_{FFT}$. This effect causes a phase difference between the guard interval and corresponding rear part of an OFDM symbol, which is seperated by N_{FFT} samples. Therefore, the signal must be derotated by the amount of the coarse $FCFO$

$$y[n] = \sum_{i=0}^{N-1} x[n] e^{-j2\pi\epsilon_{f_c} i/N_{FFT}}.$$

Symbols of the derotated signal are processed in pairs to obtain the fine CFO. The

[2] STO and CFO can be estimated in the time and the frequency domains. Another method for the estimation of STO and CFO is based on the use of training symbols in the time domain.

guard interval parts of the pairs of symbols are removed before FFT is performed. Estimation of $ICFO$, ϵ_I is an intermediate step between FFT and $FCFO$ estimation. TMCC subcarriers and pseudo-random bits corresponding to the locations of TMCC subcarriers are used to estimate $ICFO$.

Although the number of TMCC carriers changes depending on the transmission mode as presented in Table 2.3, locations of TMCC carriers in an OFDM segment do not change. The number of carriers also changes with the transmission mode. Table 2.3 shows that there are 5167 active carriers per OFDM segment for mode 3. These carriers, including scattered, continual, and TMCC pilots are DBPSK modulated according to PRBS. As displayed in Figure 4.3, all signals except the synchronization byte are EX-OR'ed. Depending on the position, each bit takes the value of $4/3$ for 1 or $-4/3$ for 0.

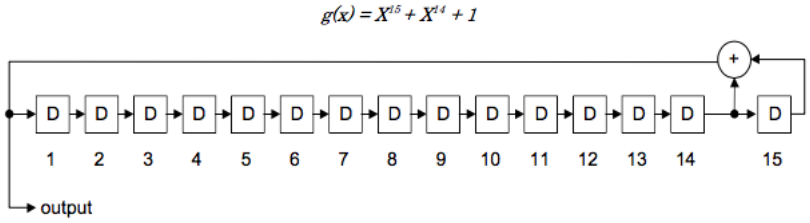

Figure 4.3 – PRBS generating polynomial and circuit [*ARIB STD-B31* , 2005].

$ICFO$ can be estimated by checking the correlation of FFT outputs of each symbol along the TMCC carriers which are weighted by PRBS

$$\Gamma[m] = \sum_{i}^{M-2} w(T[i])Y[T[i]+m] \cdot w(T[i+1])Y*[T[i+1]+m], \tag{4.3}$$

where $T[i]$ denotes the TMCC carrier, and $w[T[i]]$ is the weighting for the corresponding bit in PRBS [*Larroca et al.*, 2016]. This correlation is maximized at $m = \epsilon_I$. This step helps to make sure of the exact locations of TMCC carriers.

After removal of the guard interval and estimation of $ICFO$, each symbol can be written as

$$z_{\ell,k} = \frac{1}{\sqrt{N}} \sum_{n=0}^{N_{FFT}-1} x[n] \exp(j2\pi n(\epsilon_{I_\ell} + \epsilon_{f_c})(N_g + \ell(N_{FFT} + N_G)/N_{FFT}).$$

Considering the midpoint of K active carriers as index $k = 0$, the left half will have the indices $k \in [-(K-1)/2, 0)$, and right half will be composed of the indices $k \in (0, (K-1)/2]$. Distributing M TMCC pilots equally around $k = 0$, we will have $M_1 = M_2 = (M-1)/2$ TMCC pilots for the left (denoted by 1) and the right (denoted by 2) halves, respectively. After correlating FFT output of two sequential symbols temporally [*Fechtel*, 2000; *Speth et al.*, 2001]

$$y_{\ell,k} = z_{\ell,k} \cdot z^*_{\ell-1,k},$$

we obtain the phases of each half

$$\varphi_{\ell,1|2} = \arg \left[\sum_{k \in M_{1|2}} y_{\ell,k} \right]. \tag{4.4}$$

Using these phases we obtain $FCFO$, ϵ_{f_f} given by

$$\hat{\epsilon}_{f_f} = \frac{1}{2\pi(1 + N_g/N)} \cdot \frac{\varphi_{\ell,1} + \varphi_{\ell,2}}{2}.$$

4.5 Estimation of Sampling Clock Offset

Another synchronization issue in OFDM systems arises from the difference between the sampling frequencies applied at the transmitter and the receiver. This difference, the sampling clock offset (SCO), can be expressed as

$$\zeta = \frac{f_{s_t} - f_{s_r}}{f_{s_t}},$$

where f_{s_t} and f_{s_r} are the sampling frequencies at the transmitter and the receiver, respectively.

Differences in sampling rates at the transmitter and receiver will cause a phase difference, and thus the sampling instants will not be different from the optimal ones by a constant time [*Yang et al.*, 2000b, a]. Although the differences are small compared to STO and CFO, the sampling clock offset will cause a phase rotation in frequency domain, the same as in STO. This rotation is proportional to the timing offset and the subcarrier

index. As the effect of this phase offset is so small, it is considered to be included in *STO* [*Cho et al.*, 2010]. In this study, it is found to be largest/lowest at ±2 parts per million (ppm), which corresponds to approximately 16 samples per second. *SCO* is obtained using the phases in Equation (4.4)

$$\hat{\zeta} = \frac{1}{2\pi(1 + N_g/N)} \cdot \frac{1}{K} \cdot \frac{\varphi_{\ell,2} - \varphi_{\ell,1}}{2}.$$

4.6 Extraction of Pilot Carriers

After determining *CCFO*, *FCFO*, *SCO*, and *STO*, we take the average of each and the whole data set is derotated

$$y[n] = \sum_{n=0}^{N-1} x[n + \theta] e^{-j2\pi\epsilon n/N_{FFT}},$$

where $\epsilon = \epsilon_{f_c} + \epsilon_{f_f}$

From the final derotation step, the data is processed on a symbol-basis. After the cyclic prefix is removed, FFT is performed on the OFDM symbol. *ICFO* is estimated for one more time to determine the exact locations of TMCC carriers before moving to the next step, when the symbol index is estimated using the PRBS and scattered pilot carriers.

The initial value of the PRBS circuit must be "100101010000000" and be initialized at every OFDM frame, and it also determines the starting phase of each segment. These initial values for each segment and transmission mode are given in [Table 3-16, *ARIB STD-B31*, 2005]. The modulation is performed using the scheme

$$Re\{c_{m,l,k}\} = \frac{4}{3} \cdot 2 \cdot (\frac{1}{2} - w_k),$$

where w_k is the PRBS sequence. Here, c is the complex signal of scattered (or continual) pilots, sub-indices m, l, and k are the frame index, the OFDM symbol index, and the position of the scattered pilot position, respectively. Thus, PRBS is superimposed on the OFDM signal. Energy dispersion along the frequency band is also performed by PRBS [*ARIB STD-B31*, 2005].

For each symbol, the phase difference between the adjacent pilot carriers at 52 TMCC carrier locations is checked. Then, the in-phase and quadrature components of the symbol are coherently integrated separately. The index yielding the maximum amplitude after the coherent integration gives the location of the pilot carrier of the lth symbol. In addition to the amplitude of the pilot carrier, those of the scattered pilot (SP) carriers are also needed and are ordered in a periodic manner. The locations of the SP carriers repeat every 4 OFDM symbols. The pattern is given by

$$k = K_{min} + 3 \cdot (l \, mod 4) + 12p, \tag{4.5}$$

where p is a positive integer, and $k \in [K_{min} : K_{max}]$ where $K_{min} = 0$ for all transmission modes, and $K_{max} = 6816$ for mode 3 and $K_{max} = 1704$ for mode 1. This pattern is shown in Figure 4.4 and can be compared with the pattern in Figure 2.8. Following this pattern, the locations and magnitudes of the scattered pilot carriers in $l-th$ symbol are determined. For each symbol in a set of 4 symbols, all scattered pilot carriers are coherently integrated in every 12 active carriers in the carrier direction. Among these 4 symbols, the one with maximum magnitude is selected and fed into the last step in Figure 4.1. The symbols must follow the order of $0, 1, 2, 3$.

Starting from the estimation of the symbol index location in the previous step, all SP carriers located at every 12 active carriers are integrated after multiplying each with its corresponding bit in the PRBS sequence.

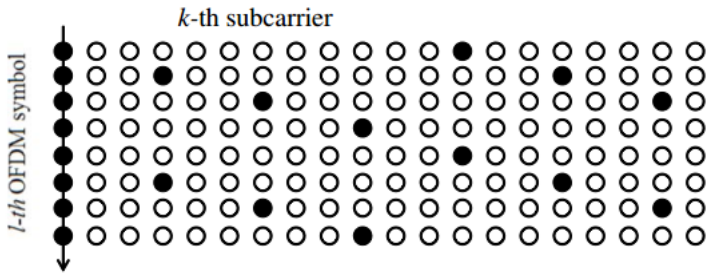

Figure 4.4 – Scattered pilot pattern [*ARIB STD-B31*, 2005].

After synchronization and the procedure to extract the symbols are performed, the in-phase and quadrature components of the symbol are obtained.

4.7 Results

The steps described above were performed on the signal recorded by an ETTUS receiver in Rio de Janeiro, Brazil. The transmitter and the receiver were stationary. Thus, no Doppler effect is considered in this research. So, the received signal is expected to have constant amplitude and phase. This prior knowledge will be used to check the performance of the synchronization algorithm developed in this research.

The search algorithm in Section 4.2 determines the data length as 8192 and guard interval as 512. ISDB-T OFDM signal data is stored in data files, each of which contains $1,048,576$ samples. After resampling the data file at a rate of $64/63$, the number of samples increases to $1,065,220$. As there is STO and the length of the data file is not divisible by the total symbol length, i.e., $8192 + 512 = 8704$, it is important to make sure there is a smooth transition between sequential files. Otherwise, the signal will have a discontinuity, as seen in Figure 4.5.

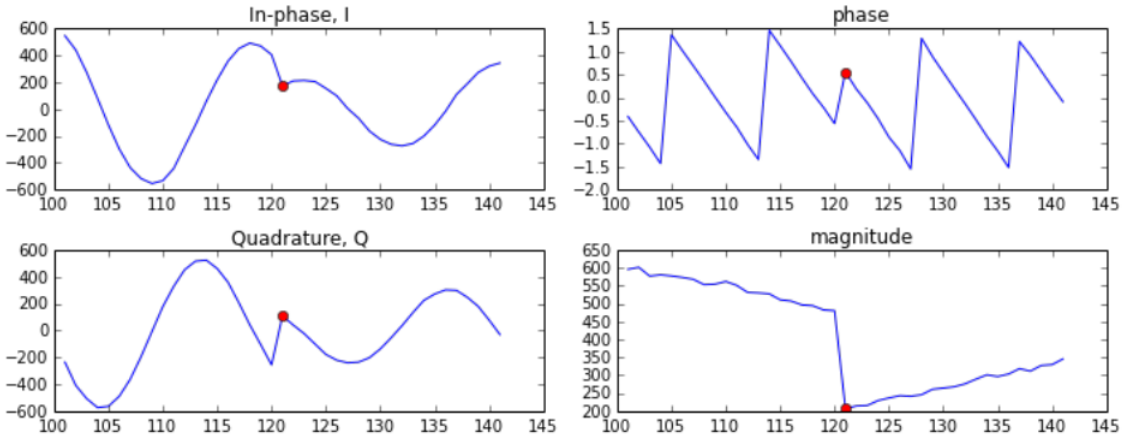

Figure 4.5 – In-phase, and quadrature components of the recorded ISDB-T data with phase and magnitude information. Only two sequential files are displayed for a better resolution of discontinuity. These plots contain the effects of frequency offsets.

The signal studied is approximately 1.29 seconds long and is obtained by processing 10 files of data. The total number of symbols is 1221. Figures 4.6 and 4.7 show the plots of in-phase, quadrature components and magnitude and phase of all symbols when no resampling is performed.

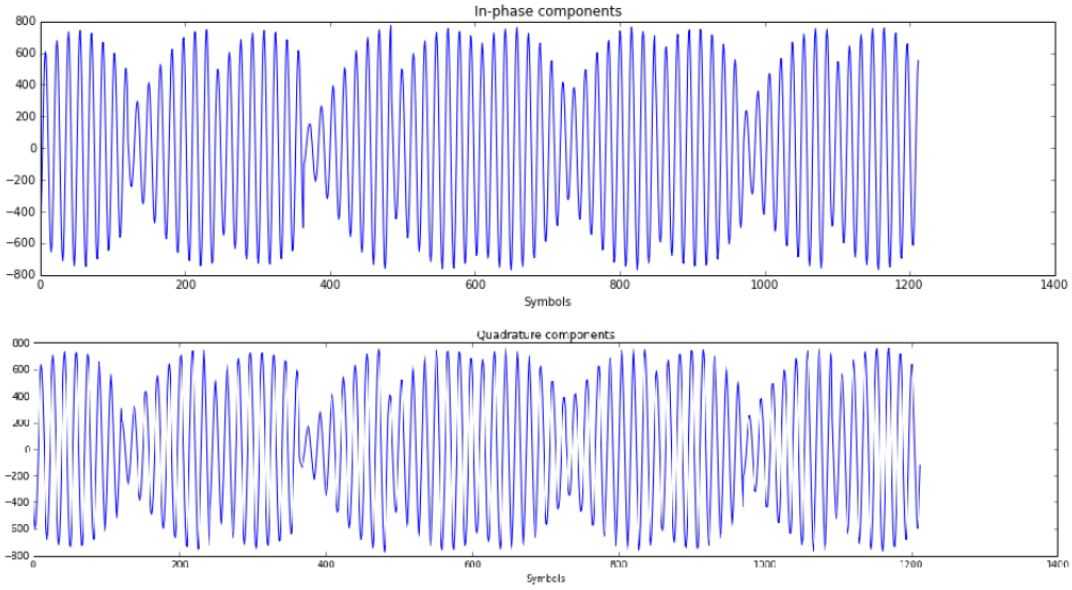

Figure 4.6 – In-phase and quadrature components of all symbols without resampling.

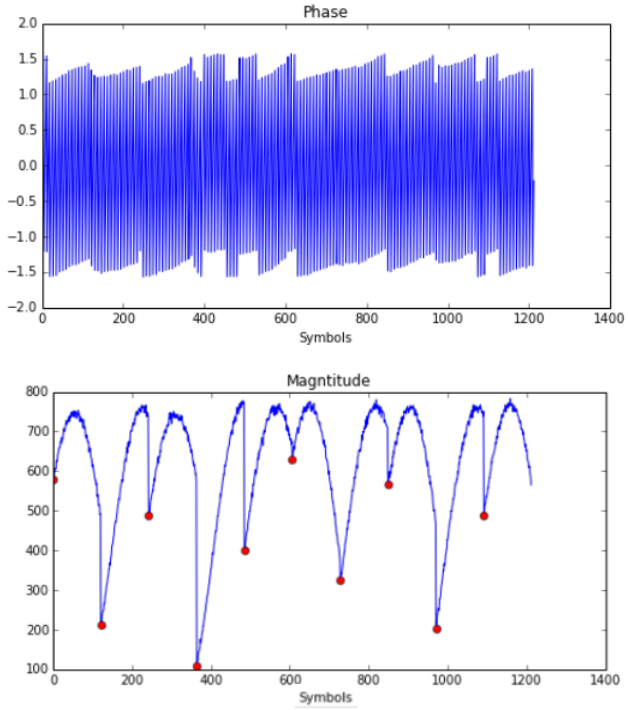

Figure 4.7 – Phase and magnitude of all symbols without resampling.

In order to ensure continuity among the files, the recorded ISDB-T data in these 10 files are stored in one array. A resampling tool which is available online was used as

mentioned in Section 4.2. This tool performs well, as demonstrated in Figures 4.8 and 4.9. Ten sequential data files are shown in Figure 4.8 to be continuous after using the resampling tool. Figure 4.9 shows that magnitude is continuous after using the resampling tool, whereas phase has discontinuities and oscillations.

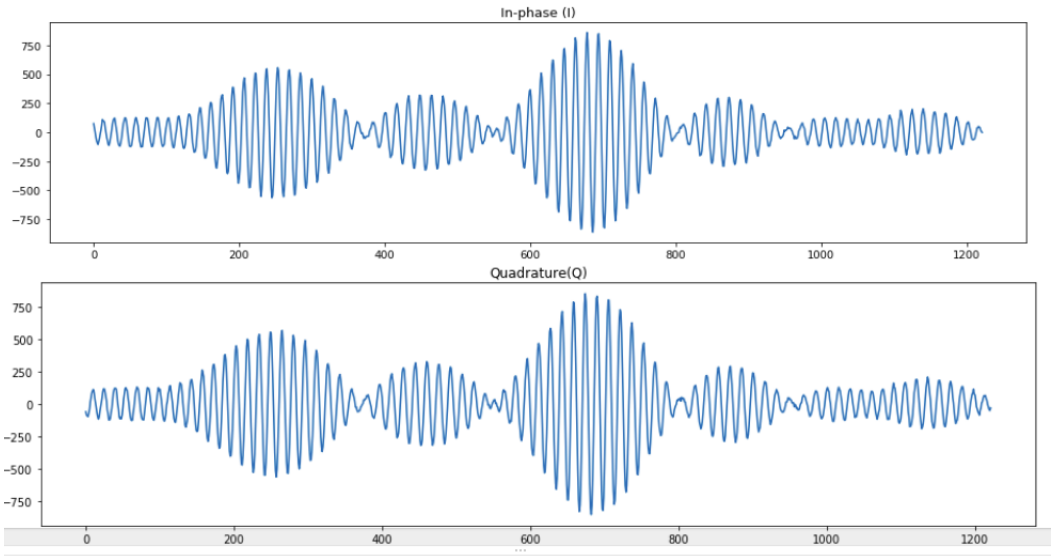

Figure 4.8 – In-phase and quadrature components of all ISDB-T symbols after resampling is performed.

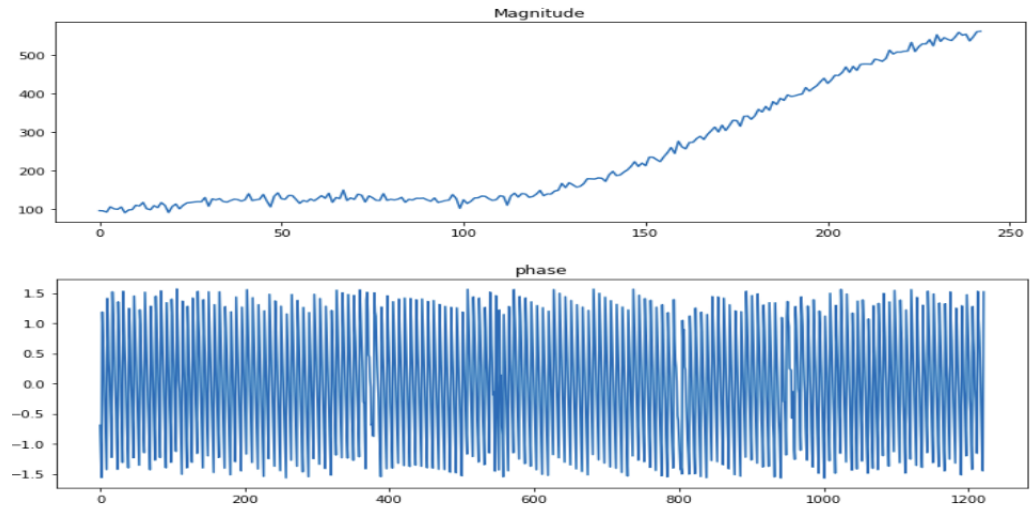

Figure 4.9 – Magnitude and phase of all ISDB-T symbols after resampling is performed.

Although magnitude is now continuous, the oscillatory in-phase and quadrature pat-

terns as well as oscillating and non-continuous phase patterns show the effects of possible carrier frequency offset.

The full receiver synchronization algorithm shown in Figure 4.1 in Section 4.1 has been discussed. The results obtained from running the algorithm are presented in the following figures. The in-phase and quadrature components along the extracted symbols are shown in Figure 4.10. The magnitude and phase are shown in Figures 4.11 and 4.12, respectively. Phase is shown to be almost constant with a mean value of approximately 2.81 radians with a variance of 0.0086 radians. The recovered amplitude is constant to within around 0.64 dB. These minor amplitude and phase changes are expected for a fixed propagation geometry under line-of-sight conditions. These findings show that the synchronization algorithm is effective.

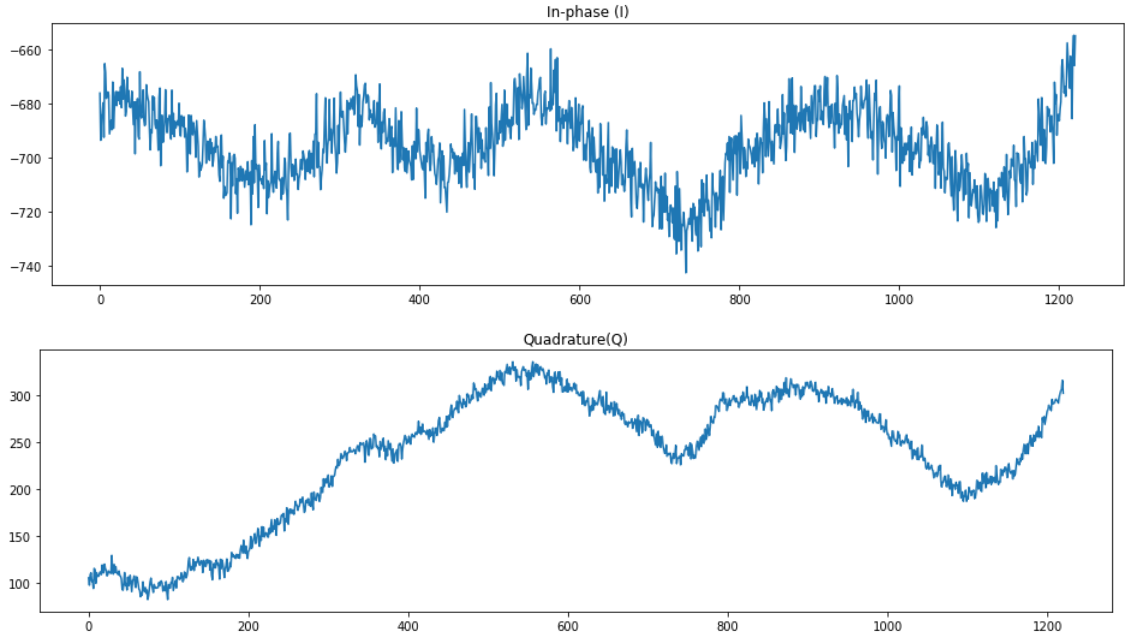

Figure 4.10 – In-phase and quadrature components of all symbols.

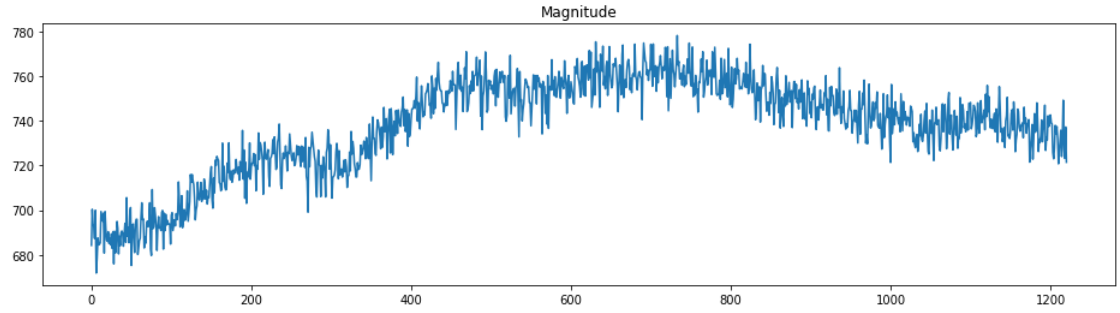

Figure 4.11 – Magnitude of all symbols.

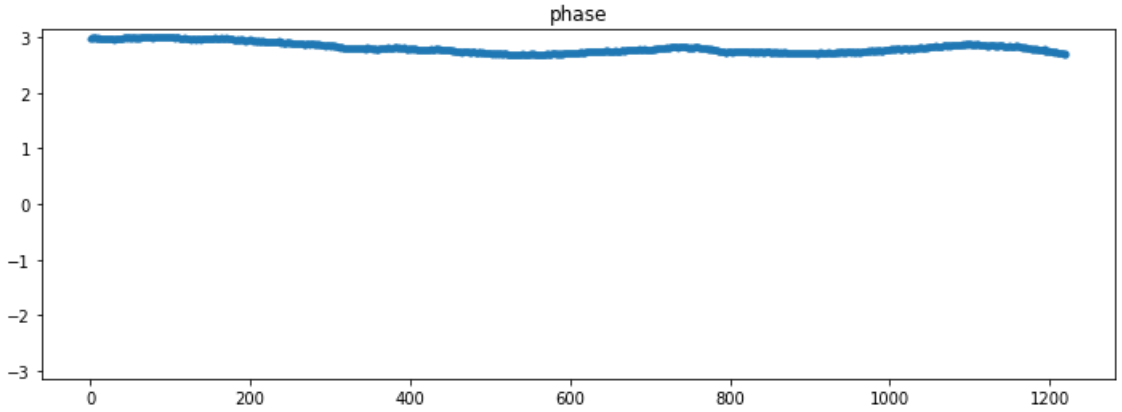

Figure 4.12 – Phase of all symbols.

CHAPTER 5

CONCLUSION AND FUTURE WORK

ISDB-T signals were selected for this research, because, as shown in Figure 2.5, ISDB-T digital television broadcasting format has been adopted by a majority of South American countries. As ISDB-T signals were recorded at a sampling rate different from the standard sampling frequency, signals were resampled. A compact full receiver synchronization algorithm was developed for this research and was applied to the resampled ISDB-T signals, and the process is detailed in a block diagram in Figure 4.1. The results provided in Section 4.7 demonstrate that the developed algorithm performs well.

In a larger context, the ultimate goal of this research was to develop an algorithm that can be utilized to synchronize the trans-ionospheric digital television signals received by a satellite-borne receiver. This goal can be achieved by realizing the following steps in the future. The parametric offset estimation and compensation algorithm developed for this research needs to be expanded and tested so as to cover other digital television broadcasting formats. Then, it should be organized so that it can estimate the types, modes and parameters of signal in any digital television broadcast format.

In addition, the proposed algorithm requires further development to account for Doppler and channel effects. Doppler shift causes a carrier frequency offset, and thus leads to a phase shift in the time domain. This phase shift should be compensated for by a moving-average filter in which initial Doppler estimation can be performed by exploiting knowledge of the satellite trajectory and the pre-selected transmitter location.

The signal received by the satellite will be distorted by the ionospheric channel. Estimation and compensation for the channel effects should be performed so that the transmitted

transionospheric digital television signal is fully recovered. Variations in the electron density create random variations in the signal phase and intensity. These fading effects can be categorized as slow and fast in the time domain which correspond to large-scale and small-scale fading in the space domain. Different fading regimes may require different statistics for channel estimation. While a lognormal or Gaussian distribution may be used for slow-fading channels, a Rayleigh or Rician distribution which also includes line-of-sight components of the incoming wave may be prefered to model the fast-fading ionospheric channel. More information on this topic can be found in *Yeh and Liu* [1982], one of the most cited papers in the field of scintillation of transionospheric radio waves.

The scintillation index, which is a function of the refractive index, shows the degree of amplitude and phase fluctuations of the radio waves. Based on different ranges of the scintillation index, the synchronization algorithm can be tested against small-, moderate- and large-scale irregularities. A detailed description of how to determine the key parameters to model such an environment can be found in *Blaunstein and Christodoulou* [2007], *Blaunstein and Plohotniuc* [2008], and *Blaunstein et al.* [2013].

The design of this ionospheric model also requires establishing a propagation geometry between a ground DTV transmitter and a satellite as well as the propagation medium in between. Therefore, after determining a DTV transmitter on Earth in geodetic coordinates, the orbital path of the satellite should be modeled using a simplified general perturbation model described in *Vallado et al.* [2006]. A model of the propagation will be completed by creating a magnetized ionospheric medium.

Following the establishment of a propagation geometry and medium, propagation of digital television signals in the ionosphere can be modeled. These two models will be excellent tools to observe the effects of perturbed ionosphere on DTV signals. Finally, the compact receiver synchronization algorithm developed for this research, which requires further expansion, can be applied to trans-ionospheric DTV signals for a comparison of the amplitudes and phases of the signals with the same signals at the ground level.

REFERENCES

Aarons, J., H. Whitney, and R. Allen (1971), Global morphology of ionospheric scintillations, *Proceedings of the IEEE*, *59*(2), 159–172.

ARIB STD-B31 (2005), Transmission system for digital terrestrial television broadcasting, *Association of Radio Industries and Businesses (ARIB) STD-B31*.

Aveiro, H., and J. Huba (2013), Equatorial spread-F studies using SAMI3 with two-dimensional and three-dimensional electrostatics, in *Annales Geophysicae*, vol. 31, pp. 2157–2162, Copernicus GmbH.

Aveiro, H., and D. Hysell (2010), Three-dimensional numerical simulation of equatorial F-region plasma irregularities with bottomside shear flow, *Journal of Geophysical Research: Space Physics*, *115*(A11).

Aveiro, H., and D. Hysell (2012), Implications of the equipotential field line approximation for equatorial spread-F analysis, *Geophysical Research Letters*, *39*(11).

Bahcivan, H., and R. Novoselov (2016), Ionospheric scintillation explorer (ISX): Science payload, Menlo Park, CA.

Blaunstein, N., and C. Christodoulou (2007), *Radio propagation and adaptive antennas for wireless communication links: terrestrial, atmospheric and ionospheric*, John Wiley & Sons.

Blaunstein, N., and E. Plohotniuc (2008), *Ionosphere and applied aspects of radio communication and radar*, CRC press.

Blaunstein, N., S. Pulinets, and Y. Cohen (2013), Computation of the key parameters of radio signals propagating through a perturbed ionosphere in the land-satellite channel, *Geomagnetism and Aeronomy*, *53*(2), 204–215.

Cho, Y. S., J. Kim, W. Y. Yang, and C. G. Kang (2010), *MIMO-OFDM wireless communications with MATLAB*, John Wiley & Sons.

DVB (2017), Digital terrestrial television systems, `https://www.dvb.org/resources/public/images/site/dvb-t2_map.pdf`.

Fechtel, S. A. (2000), OFDM carrier and sampling frequency synchronization and its performance on stationary and mobile channels, *IEEE Transactions on Consumer Electronics*, *46*(3), 438–441.

Galli, S., H. Koga, and N. Kodama (2008), Advanced signal processing for PLCs: Wavelet-OFDM, pp. 187 – 192, doi:10.1109/ISPLC.2008.4510421.

Garmatyuk, D., and K. Kauffman (2009), Radar and data communication fusion with UWB-OFDM software-defined system, in *2009 IEEE International Conference on Ultra-Wideband*, pp. 454–458, IEEE.

Goldsmith, A. (2005), *Wireless communications*, Cambridge University Press.

Haykin, S., and M. Moher (2005), *Modern wireless communications*, Prentice Hall.

Hey, J., S. Parsons, and J. Phillips (1946), Fluctuations in cosmic radiation at radio-frequencies, in *Classics in Radio Astronomy*, pp. 228–230, Springer.

Huba, J., G. Joyce, and J. Krall (2008), Three-dimensional equatorial spread-F modeling, *Geophysical Research Letters*, *35*(10).

Iuliano, J., and H. Bahcivan (2015), Ionospheric Scintillation Explorer (ISX), *AGU Fall Meeting Abstracts*, EP53C-1044.

Jursa, A. S., et al. (1985), *Handbook of geophysics and the space environment*, NTIS.

Keskinen, M., S. Ossakow, S. Basu, and P. Sultan (1998), Magnetic-flux-tube-integrated evolution of equatorial ionospheric plasma bubbles, *Journal of Geophysical Research: Space Physics*, *103*(A3), 3957–3967.

Keskinen, M., S. Ossakow, and B. G. Fejer (2003), Three-dimensional nonlinear evolution of equatorial ionospheric spread-F bubbles, *Geophysical Research Letters*, *30*(16).

Langton, C. (2004), Orthogonal frequency division multiplex (OFDM) tutorial.

Larroca, F., P. F. Guridi, G. G. Sena, V. Gonzalez-Barbone, and P. Belzarena (2016), An open and free isdb-t full_seg receiver implemented in GNU radio, *WInnComm*.

Levanon, N. (2000a), Multifrequency complementary phase-coded radar signal, *IEE Proceedings-Radar, Sonar and Navigation*, *147*(6), 276–284.

Levanon, N. (2000b), Multifrequency radar signals, in *Record of the IEEE 2000 International Radar Conference [Cat. No. 00CH37037]*, pp. 683–688, IEEE.

Liu, P., B.-b. Li, Z.-y. Lu, and F.-k. Gong (2004), A new frequency synchronization scheme for OFDM, *IEEE Transactions on Consumer Electronics*, *50*(3), 823–828.

Mosier, R., and R. Clabaugh (1958), Kineplex, a bandwidth-efficient binary transmission system, *Transactions of the American Institute of Electrical Engineers, Part I: Communication and Electronics*, *76*(6), 723–728.

Muschallik, C. (1995), Influence of RF oscillators on an OFDM signal, *IEEE transactions on Consumer Electronics*, *41*(3), 592–603.

Pollet, T., P. Spruyt, and M. Moeneclaey (1994), The BER performance of OFDM systems using non-synchronized sampling, in *1994 IEEE GLOBECOM. Communications: The Global Bridge*, pp. 253–257, IEEE.

Pollet, T., M. Van Bladel, and M. Moeneclaey (1995), BER sensitivity of OFDM systems to carrier frequency offset and Wiener phase noise, *IEEE Transactions on Communications*, *43*(234), 191–193.

Putnam, W., and J. Smith (1997), Design of fractional delay filters using convex optimization, in *Applications of Signal Processing to Audio and Acoustics, 1997. 1997 IEEE ASSP Workshop on*, pp. 4–pp, IEEE.

Reed, J. (2005), *Introduction to ultra wideband communication systems*, Prentice Hall.

Retterer, J. (2010), Forecasting low-latitude radio scintillation with 3-d ionospheric plume models: 1. plume model, *Journal of Geophysical Research: Space Physics*, *115*(A3).

Sandell, M., D. McNamara, and S. Parker (2005), Frequency offset tracking for MIMO OFDM systems using pilots, in *IEEE Wireless Communications and Networking Conference, 2005*, vol. 1, pp. 7–11, IEEE.

Sit, Y. L., C. Sturm, L. Reichardt, T. Zwick, and W. Wiesbeck (2011), The OFDM joint radar-communication system: An overview, in *Proc. Int. Conf. Advances in Satellite and Space Communications (SPACOMM 2011)*, pp. 69–74.

Speth, M., D. Daecke, and H. Meyr (1998), Minimum overhead burst synchronization for OFDM based broadband transmission, in *IEEE GLOBECOM 1998 (Cat. NO. 98CH36250)*, vol. 5, pp. 2777–2782, IEEE.

Speth, M., S. Fechtel, G. Fock, and H. Meyr (2001), Optimum receiver design for OFDM-based broadband transmission. ii. a case study, *IEEE Transactions on Communications*, *49*(4), 571–578.

Sturm, C., and W. Wiesbeck (2011), Waveform design and signal processing aspects for fusion of wireless communications and radar sensing, *Proceedings of the IEEE*, *99*(7), 1236–1259.

Sturm, C., L. Reichardt, T. Zwick, and W. Wiesbeck (2009), Evaluation of beam-forming algorithms for automotive ofdm signal based radar, in *2009 European Radar Conference (EuRAD)*, pp. 141–144, IEEE.

Tatarskii, V., A. Ishimaru, and V. Zavorotny (1993), Wave propagation in random media (scintillation), in *Wave Propagation in Random Media (Scintillation)*.

Vallado, D., P. Crawford, R. Hujsak, and T. Kelso (2006), *Revisiting Spacetrack Report #3*, doi:10.2514/6.2006-6753.

van Nee, R., and R. Prasad (2000), *OFDM for wireless multimedia communications*, Artech House, Inc.

Yang, B., K. B. Letaief, R. S. Cheng, and Z. Cao (2000a), Timing recovery for OFDM transmission, *IEEE Journal on Selected Areas in Communications*, *18*(11), 2278–2291.

Yang, B., Z. Ma, and Z. Cao (2000b), Ml-oriented DA sampling clock synchronization for OFDM systems, in *Communication Technology Proceedings, 2000. WCC-ICCT 2000. International Conference on*, vol. 1, pp. 781–784, IEEE.

Yeh, K. C., and C.-H. Liu (1982), Radio wave scintillations in the ionosphere, *Proceedings of the IEEE*, *70*(4), 324–360.

Zaidi, A. A., R. Baldemair, H. Tullberg, H. Bjorkegren, L. Sundstrom, J. Medbo, C. Kilinc, and I. Da Silva (2016), Waveform and numerology to support 5g services and requirements, *IEEE Communications Magazine*, *54*(11), 90–98.